

# Sliding Mode Guidance and Control for UAV Carrier Landing

SEOKWON LEE   
JIHOON LEE   
SOMANG LEE   
HYUNJIN CHOI 

YODAN KIM , Senior Member, IEEE  
Seoul National University, Seoul, South Korea

SEUNGKEUN KIM, Senior Member, IEEE  
JINYOUNG SUK

Chungnam National University, Daejeon, South Korea

**A guidance and control system is proposed for automatic carrier landing of an unmanned aerial vehicle (UAV). To this end, the position and attitude of the carrier is predicted by considering the sea state so that the UAV guidance loop can be compensated during the final approach phase. The landing kinematics and reference trajectory are determined using the predicted touchdown position. Nonlinear guidance and control laws are designed based on a sliding-mode control scheme to make the UAV robustly follow the reference trajectory.**

Manuscript received January 16, 2017; revised December 29, 2017, February 28, 2018, and July 4, 2018; released for publication July 29, 2018. Date of publication August 27, 2018; date of current version April 11, 2019.

DOI. No. 10.1109/TAES.2018.2867259

Refereeing of this contribution was handled by Y. B. Shtessel.

This study was supported by the Guidance/Control Study for Take-off and Landing on a Ship program through the Agency for Defense Development (ADD) of South Korea under the Grant UD1130053JD.

Authors' addresses: Seokwon Lee, J. Lee, Somang Lee, H. Choi, and Y. Kim are with the Institute of Advanced Aerospace Technology, Department of Mechanical and Aerospace Engineering, Seoul National University, Seoul 08826, South Korea, E-mail: (blueswl@snu.ac.kr; leejihoon@snu.ac.kr; cjsomang@snu.ac.kr; lightsai@daum.net; ydkim@snu.ac.kr); S. Kim and J. Suk are with the Department of Aerospace Engineering, Chungnam National University, Daejeon 34134, South Korea, E-mail: (skim78@cnu.ac.kr; jsuk@cnu.ac.kr). (Corresponding author: Yodan Kim.)

0018-9251 © 2018 IEEE

## NOMENCLATURE

$\mathbf{r}_{\text{uav}}$	UAV position.
$\mathbf{r}_s$	Carrier position.
$\mathbf{V}_s$	Carrier velocity.
$\mathbf{r}_{\text{uav}/s}$	Relative position of the UAV with respect to carrier.
$\mathbf{r}_{\text{ref}}$	Position of the reference trajectory.
$\mathbf{r}_{\text{ref}/s}$	Relative position of the reference trajectory with respect to carrier.
$\phi_s, \theta_s, \psi_s$	Roll, pitch, and yaw angles of the carrier by <i>seakeeping</i> motion.
$x_{\text{surge}}, y_{\text{sway}}, z_{\text{heave}}$	Surge, sway, and heave motion by <i>seakeeping</i> motion.
$V_s, \chi_s$	Speed and heading angle of the carrier
$\lambda, \eta$	Elevation and azimuth angles of the glide path.
$d$	Distance between the UAV and the carrier.
$\lambda_c, \eta_c, d_c$	Desired glide-path angles and distance between the UAV and carrier.
$V, \chi, \gamma$	Speed, heading, and flight-path angle of the UAV.
$\alpha, \beta, \mu$	Angle-of-attack, sideslip, and roll angle of the UAV.
$\ \mathbf{x}\  = \sqrt{\mathbf{x}^T \mathbf{x}}$	Euclidian norm of a vector.

## I. INTRODUCTION

Landing aircraft on a carrier is one of the most difficult tasks in naval air operations. Throughout the landing procedure, aircraft should tightly follow the glide slope while maintaining the approaching speed to land on a narrow touchdown area. Combined with undesirable environmental conditions, such as low visibility, turbulent winds, high sea state, and the risky deck motion, the performance requirements of the landing become extremely difficult to be satisfied. In fact, the U.S. Navy announced that most of the accidents between 1947 and 1988 are concentrated on takeoff and landing operations, and they are closely related to human factors [1]. To address this difficulty, the development of an autonomous system for the carrier landing has emerged as a major concern to replace the manned controlled system, and appropriate guidance and control laws are required to achieve the precision landing on a carrier deck.

Over the past decades, considerable guidance and control laws have been suggested for automatic carrier landing system (ACLS) [2]–[12]. The classical ACLS uses both the shipboard computer from the carrier and the autopilot at the aircraft for fully automatic approach and landing. In the shipboard system, h-dot guidance generates a pitch command to capture the glide path. The command is transmitted back to the aircraft through a radio frequency data link [2], [5]. In the autopilot of the aircraft, control augmentation system (CAS) is designed to track the pitch angle command meanwhile approach power compensator system (APCS) controls the engine throttle to maintain trimmed angle of attack [8]–[12]. Using a predefined control

architecture, parameter optimization [13], [14] and linearized aircraft modeling technique considering an air-turbulence model [15] were suggested. Subrahmanyam [10] suggested a robust controller using H-infinity synthesis for the F-18 aircraft, and Niewoehner and Kaminer [11] applied the H-infinity controller to the F-14 aircraft. However, the conventional approach only considers longitudinal motion of the aircraft and ship with linearized dynamics, which cannot fully reflect the three-dimensional (3-D) relative motion between the aircraft and the ship. Therefore, the accuracy of touchdown in ACLS may be degraded. Furthermore, the ACLS highly depends on shipboard data, which is vulnerable to communication problems in the shipboard broadcasting system.

For safe landing under harsh weather conditions, an ACLS should be robust with respect to air turbulence and deck fluctuations. As a matter of fact, only a small change in the deck height can lead to a significant horizontal position error along the desired landing site. For this reason, deck motion compensation (DMC) is crucial in the *touchdown phase*. In conventional systems, DMC requires stabilized shipboard signals [3], [10], [16]. However, the conventional DMC may be dangerous in case of communication failures. To address this issue, several approaches have been suggested in which the unmanned aerial vehicle (UAV) could perform onboard DMC [6], [17], and considerable research has proposed carrier motion prediction algorithms [18]–[20]. In [19], pitch and heave dynamics of the ship motion under wave excitation were obtained by power spectral density analysis, and the extended Kalman filter was applied to predict the pitch/heave motion. Most of the research, however, considered the vertical motion of the center of gravity of the carrier instead of deck motion at the touchdown point. Therefore, the generic motion at the touchdown position should be considered, and a suitable DMC should be designed for accurate landing. Boskovic and Redding [6] proposed a deck motion prediction algorithm based on an autoregressive model and a Kalman filter using a simple UAV kinematic model.

This study proposes guidance and control laws for precision ACLS. It is assumed that the carrier position, which is disturbed by wave excitation, is received in shipboard sensors. First, the inertial-frame 3-D landing kinematics is derived based on the relative geometry. In the guidance system, a reference trajectory is generated to represent a virtual glide path. To follow the 3-D glide path, a landing-guidance law is designed using a sliding-mode control (SMC). Since SMC is known to be robust to uncertainties, there have been lots of applications for missiles [21], [22], robot manipulators [23], satellites [24], and UAVs [25]–[27]. To enhance the accuracy of the guidance scheme during *touchdown phase*, a DMC is proposed considering the terminal position of the carrier. The predicted carrier deck motion is used to correct glide path. In the control system, a nonlinear dynamics of the UAV is considered and a SMC is applied to control the flight-path angle and UAV speed.

The main contributions of this paper can be summarized as follows. First, novel 3-D nonlinear guidance and control laws based on a SMC scheme are proposed. Compared to the conventional ACLS, the proposed method not only deals with 3-D landing but also has unique guidance-control structure, where the flight-path angles and speed are directly controlled without command conversion that the APCS necessitates. Second, a deck-motion prediction algorithm is designed for UAV landing. Using the algorithm, UAV can correct the desired touchdown position with less dependence on the shipboard signal, and the landing accuracy can be enhanced by considering both the relative landing geometry and configuration of the landing spot on the ship. To demonstrate the effectiveness of the proposed method, numerical simulation is performed. Through numerical simulation, the performance of the proposed ACLS and DMC is demonstrated and compared with the performance of the conventional ACLS.

The remainder of the paper is organized as follows. Section II describes the problem statement and landing geometry. Section III presents the guidance design and DMC algorithm. Section IV provides the controller design, and the numerical simulation is presented in Section V. Section VI gives the conclusions.

## II. PROBLEM STATEMENT

### A. Problem Formulation

For ACLS, this section explains the carrier landing sequence of an UAV. The landing sequence consists of two phases; the *approach and descent phase* and the *touchdown phase* [28]. In the *approach and descent phase*, which is the first part of the landing sequence, the UAV approaches a designated point, i.e., marshal point, and descends following the reference glide path. In case the shipboard navigation is unavailable, the UAV should be able to estimate the carrier states by itself. In this study, it is assumed that the position of the carrier center is available by shipboard sensors, and the UAV should carry out relative navigation by using the received position and on-board data. As the position of the carrier transmitted from the ship-board is different from the desired landing site, an accommodation logic is required for the UAV landing. In *touchdown phase*, the UAV should precisely land on the fluctuating landing site of the deck. Indeed, within the short runway, the UAV should stop with very short braking distance. To cope with these difficulties, most of the carrier landings, unlike ground landing, adopt alternative way of landing called arresting hook landing instead of the flare landing of general landing procedure at land. Upon a narrow and short landing site, the UAV approaches the desired landing site where the arresting wires are placed. And, the UAV decelerates the speed as fast as possible, with aid of the arresting wires after touchdown. Fig. 1(a) describes the landing procedure summarized as follows.

- 1) A carrier moves with constant speed and has a runway that is tilted by  $9^\circ$  from its longitudinal axis.

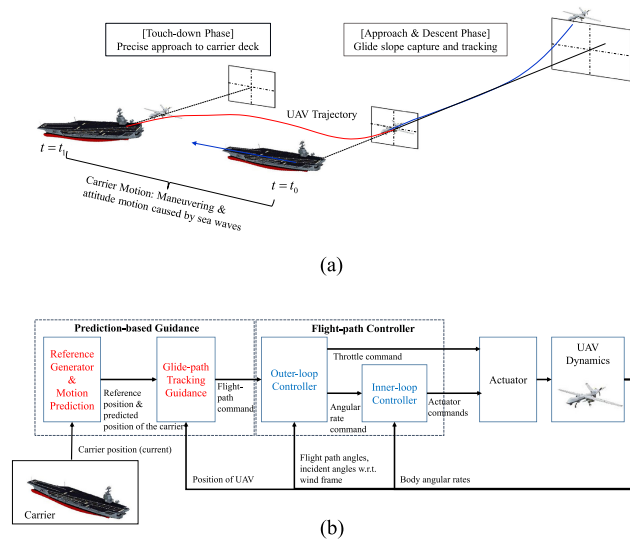


Fig. 1. Landing sequence and system architecture for ACLS.  
(a) Landing procedure. (b) ACLS architecture.

- 2) The desired touchdown position is located at the middle of the arresting wires, and the area of the allowable landing site is set to be 20 ft × 40 ft.
- 3) The ACLS has to cope with sea state 5, where the carrier motion is highly affected by sea waves.
- 4) The UAV receives the position information of the carrier center from a shipboard navigation system, but sensor noise is not considered in this study.
- 5) DMC and relative navigation should be performed in the ACLS.

Note that the landing operation is done in 3-D space and the aircraft dynamics are nonlinear and cross-coupled. Therefore, it is desirable that the relative motion in 3-D space and the nonlinear dynamics are taken into account in ACLS design. In this study, the measurement noise is not considered by assuming that the high frequency sensor noise can be sufficiently attenuated by an appropriate filter. It is reported that the touchdown error is mainly due to wind disturbances and ship fluctuation by sea wave rather than the sensor noise [8], and the ACLS should be robust with respect to the uncertainties, including the wind disturbance and time delay of signal. To accomplish the above requirements, we construct a guidance and control architecture for the ACLS, as shown in Fig. 1(b). In the guidance loop, UAV speed and flight-path angle commands are generated to make the UAV follow the glide path (*approach and descent phase*) and reach the touchdown area (*touch-down phase*), where the carrier motion is predicted to enhance the accuracy of the touchdown. In the control loop, the flight dynamics is decomposed into fast and slow dynamics under the assumption of time-scale separation, and a flight-path controller is designed using the SMC scheme.

## B. Carrier and Deck Motion

In this section, the carrier dynamics and carrier deck motion of the CVN 65 are briefly explained [29]. The motion

of the carrier center  $\mathbf{r}_{scm}$  can be decoupled into *seakeeping*, which refers to the motion affected by wave excitation, and *maneuvering* as [6], [30]

$$\begin{aligned} \dot{\mathbf{r}}_{scm} &= \mathbf{V}_{maneuver} + \mathbf{V}_{seakeep} \\ &= \begin{bmatrix} V_{ship} \cos \chi_s \\ V_{ship} \sin \chi_s \\ 0 \end{bmatrix} \\ &\quad + \begin{bmatrix} \dot{y}_{sway} \cos \chi_s - \dot{x}_{surge} \sin \chi_s \\ \dot{y}_{sway} \sin \chi_s + \dot{x}_{surge} \cos \chi_s \\ \dot{z}_{heave} \end{bmatrix} \end{aligned} \quad (1)$$

where  $(x_{surge}, y_{sway}, z_{heave})$  represent the surge, sway, and heave motion induced by the wave excitation, respectively, and  $(V_{ship}, \chi_s)$  represent the carrier speed and heading angle, respectively. The *seakeeping* motion at the carrier center due to the wave excitation can be simplified as

$$\begin{aligned} \dot{\phi}_s &= A_\phi \sin \omega_\phi t + v_\phi \\ \dot{\theta}_s &= A_\theta \sin \omega_\theta t + v_\theta \\ \dot{\psi}_s &= A_\psi \sin \omega_\psi t + v_\psi \\ \dot{x}_{surge} &= A_{surge} \sin \omega_{surge} t + v_{surge} \\ \dot{y}_{sway} &= A_{sway} \sin \omega_{sway} t + v_{sway} \\ \dot{z}_{heave} &= A_{heave} \sin \omega_{heave} t + v_{heave} \end{aligned} \quad (2)$$

where  $(A_\phi, A_\theta, A_\psi)$  and  $(\omega_\phi, \omega_\theta, \omega_\psi)$  represent the amplitude and frequency corresponding to the attitude motion,  $(A_{surge}, A_{sway}, A_{heave})$  and  $(\omega_{surge}, \omega_{sway}, \omega_{heave})$  represent the amplitude and frequency corresponding to the translation motion, which are given as statistical data [29].  $(v_\phi, v_\theta, v_\psi, v_{surge}, v_{sway}, v_{heave})$  are disturbances from high-frequency modes. These parameters vary according to the sea states. Considering the lever-arm vector  $\mathbf{p}_s$  from the center of the carrier to the location of the deck, the carrier deck motion can be obtained as a rigid-body motion

$$\begin{aligned} \mathbf{r}_s &= \mathbf{r}_{scm} + \mathbf{R}\mathbf{p}_s \\ \dot{\mathbf{r}}_s &= \dot{\mathbf{r}}_{scm} + \dot{\mathbf{R}}\mathbf{p}_s \\ &= \mathbf{V}_{maneuver} + \mathbf{V}_{seakeep} + \omega_s \times \mathbf{R}\mathbf{p}_s \end{aligned} \quad (3)$$

where  $\omega_s$  is the angular rate of the carrier, and  $\mathbf{R}$  denotes the direction cosine matrix of the carrier [6]. In order to figure out the perturbed motion at the carrier deck, let us define a seakeeping vector  $\mathbf{r}_{seakeep}$ . Then, the corresponding *seakeeping* motion at the carrier deck can be expressed as follows:

$$\begin{aligned} \mathbf{r}_{seakeep} &= \begin{bmatrix} y_{sway} \cos \chi_s - x_{surge} \sin \chi_s \\ y_{sway} \sin \chi_s + x_{surge} \cos \chi_s \\ z_{heave} \end{bmatrix} + \mathbf{R}\mathbf{p}_s \\ \dot{\mathbf{r}}_{seakeep} &= \mathbf{V}_{seakeep} + \omega_s \times \mathbf{R}\mathbf{p}_s \end{aligned} \quad (4)$$

Note that the perturbed motion describes the deviation from the nominal landing position without *seakeeping*. The perturbed motion is critical to landing accuracy because even a small vertical deviation from the deck motion will disperse

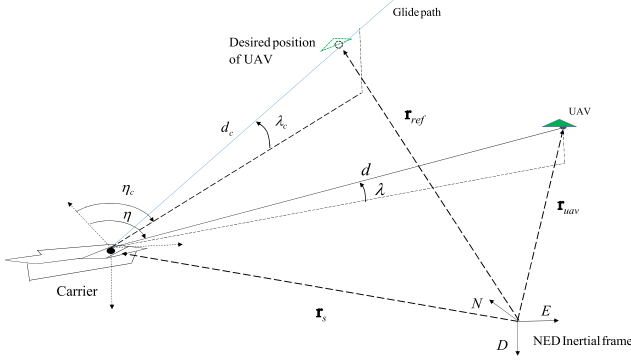


Fig. 2. Landing geometry for ACLS.

the touchdown point from the desired spot [28]. The vertical deviation by the perturbed motion of the carrier deck derived from (4) can be expressed as

$$\mathbf{r}_{\text{seakeep}}(3) = z_{\text{heave}} - \sin \theta_s p_{s,x} + \cos \theta_s \sin \phi_s p_{s,y} + \cos \theta_s \cos \phi_s p_{s,z} \quad (5)$$

where  $\mathbf{p}_s = [p_{s,x} \ p_{s,y} \ p_{s,z}]^T$  is the relative distance from the center of the carrier and the deck position. The vertical displacement from the desired landing spot is affected not only by the heave, but also the attitude of the ship, and the roll motion also affects the vertical deviation. For this reason, it is desirable that the effects of the attitude and carrier geometry is considered in DMC design.

### C. Landing Kinematics

This section derives landing kinematics to design a guidance law for ACLS. Consider the 3-D landing geometry shown in Fig. 2.  $\mathbf{r}_s$  and  $\mathbf{r}_{\text{uav}}$  denote the carrier deck position and UAV position, respectively. Note that the glide path keeps moving during the landing, and therefore, the glide-path angle needs to be defined in a relative manner. The relative point vector  $\mathbf{r}_{p/s}$  of the virtual glide slope from the carrier can be expressed as

$$\mathbf{r}_{p/s} = \begin{bmatrix} d_c \cos \lambda_c \cos \eta_c \\ d_c \cos \lambda_c \sin \eta_c \\ -d_c \sin \lambda_c \end{bmatrix} \quad (6)$$

where  $d_c$  denotes the distance between the carrier and a virtual point on the glide path, and  $\lambda_c$  and  $\eta_c$  denote the vertical elevation and horizontal azimuth angles, respectively. Using (6), a point lying on the glide path can be selected. In a similar manner, the relative position of the UAV can be expressed using parameters  $(\eta, \lambda, d)$  as

$$\mathbf{r}_{\text{uav}/s} = \mathbf{r}_{\text{uav}} - \mathbf{r}_s \quad (7)$$

where

$$\mathbf{r}_{\text{uav}/s} = [d \cos \lambda \cos \eta \quad d \cos \lambda \sin \eta \quad -d \sin \lambda]^T \quad (8)$$

Differentiating (8) with respect to  $t$  gives the relative velocity of the UAV with respect to the carrier as

$$\dot{\mathbf{r}}_{\text{uav}/s} = \frac{\partial \mathbf{r}_{\text{uav}/s}}{\partial d} \dot{d} + \frac{\partial \mathbf{r}_{\text{uav}/s}}{\partial \lambda} \dot{\lambda} + \frac{\partial \mathbf{r}_{\text{uav}/s}}{\partial \eta} \dot{\eta} \quad (9)$$

where  $\frac{\partial \mathbf{r}_{\text{uav}/s}}{\partial d}$ ,  $\frac{\partial \mathbf{r}_{\text{uav}/s}}{\partial \lambda}$ , and  $\frac{\partial \mathbf{r}_{\text{uav}/s}}{\partial \eta}$  can be obtained as

$$\begin{aligned} \frac{\partial \mathbf{r}_{\text{uav}/s}}{\partial d} &= [\cos \lambda \cos \eta \quad \cos \lambda \sin \eta \quad -\sin \lambda]^T \\ \frac{\partial \mathbf{r}_{\text{uav}/s}}{\partial \lambda} &= [-d \sin \lambda \cos \eta \quad -d \sin \lambda \sin \eta \quad -d \cos \lambda]^T \\ \frac{\partial \mathbf{r}_{\text{uav}/s}}{\partial \eta} &= [-d \cos \lambda \sin \eta \quad d \cos \lambda \cos \eta \quad 0]^T \end{aligned} \quad (10)$$

Differentiating (8) and substituting (9) into the resulting equation yields the following UAV kinematics:

$$\dot{\mathbf{r}}_{\text{uav}} = \dot{\mathbf{r}}_s + \frac{\partial \mathbf{r}_{\text{uav}/s}}{\partial d} \dot{d} + \frac{\partial \mathbf{r}_{\text{uav}/s}}{\partial \lambda} \dot{\lambda} + \frac{\partial \mathbf{r}_{\text{uav}/s}}{\partial \eta} \dot{\eta} \quad (11)$$

The objective of the landing guidance is to obtain the commands to track the relative glide path  $(d, \lambda, \eta)$ . Let us define state variable vectors  $\mathbf{x}_1 = [d \ \lambda \ \eta]^T$  and  $\mathbf{x}_2 = [V \ \chi \ \gamma]^T$ . Equation (11) can be reformulated in terms of  $\mathbf{x}_1$  and  $\mathbf{x}_2$  as

$$\mathbf{M} \dot{\mathbf{x}}_1 = -\dot{\mathbf{r}}_s + \mathbf{h}_1(\mathbf{x}_2) \quad (12)$$

where  $\mathbf{M} = [\frac{\partial \mathbf{r}_{\text{uav}/s}}{\partial d} \quad \frac{\partial \mathbf{r}_{\text{uav}/s}}{\partial \lambda} \quad \frac{\partial \mathbf{r}_{\text{uav}/s}}{\partial \eta}]$  is a Jacobian matrix of  $\mathbf{r}_{\text{uav}/s}$  and  $\dot{\mathbf{r}}_{\text{uav}}$  can be represented as follows:

$$\mathbf{h}_1(\mathbf{x}_2) = \dot{\mathbf{r}}_{\text{uav}} = V \begin{bmatrix} \cos \gamma \cos \chi \\ \cos \gamma \sin \chi \\ -\sin \gamma \end{bmatrix} \quad (13)$$

Note that  $\mathbf{x}_2$  and  $\dot{\mathbf{r}}_{\text{uav}}$  have a one-to-one correspondence, and therefore, we have

$$\mathbf{x}_2 = \mathbf{h}_1^{-1}(\dot{\mathbf{r}}_{\text{uav}}) = \begin{bmatrix} \|\dot{\mathbf{r}}_{\text{uav}}\| \\ \tan^{-1} \left( \frac{\dot{\mathbf{r}}_{\text{uav}}(2)}{\dot{\mathbf{r}}_{\text{uav}}(1)} \right) \\ -\sin^{-1} \left( \frac{\dot{\mathbf{r}}_{\text{uav}}(3)}{\|\dot{\mathbf{r}}_{\text{uav}}\|} \right) \end{bmatrix} \quad (14)$$

Therefore, pseudo-guidance input  $\mathbf{v} = \mathbf{h}_1(\mathbf{x}_2)$  can be used instead of  $\mathbf{x}_2$ . Now, the  $\mathbf{x}_1$  dynamics can be expressed as an input-affine form with respect to  $\mathbf{v}$

$$\dot{\mathbf{x}}_1 = \mathbf{f}_1 + \mathbf{g}_1 \mathbf{v}(\mathbf{x}_2) \quad (15)$$

where  $\mathbf{f}_1 = -\mathbf{M}^{-1} \dot{\mathbf{r}}_s$ , and  $\mathbf{g}_1 = \mathbf{M}^{-1}$ . Since the column vectors of  $\mathbf{M}$  are mutually orthogonal,  $\mathbf{M}$  is nonsingular.

### D. Dynamic Model

In this study, a fixed-wing UAV is considered for the automatic carrier landing. The nonlinear UAV dynamics can be represented using  $\mathbf{x}_2 = [V \ \chi \ \gamma]^T$ ,  $\mathbf{x}_3 = [\mu \ \alpha \ \beta]^T$ ,



and  $\mathbf{x}_4 = [p \ q \ r]^T$  as [25]

$$\dot{\mathbf{x}}_2 = \begin{bmatrix} -g \sin \gamma \\ 0 \\ -\frac{g}{V} \cos \gamma \end{bmatrix} + \begin{bmatrix} \frac{-D+T_{\max} \delta_r \cos \alpha \cos \beta}{m} \\ \frac{(-Y \cos \mu + L \sin \mu) + T_{\max} (\sin \alpha \sin \mu - \cos \alpha \sin \beta \cos \mu) \delta_r}{m V \cos \gamma} \\ \frac{Y \sin \mu + L \cos \mu + T_{\max} (\cos \alpha \sin \beta \sin \mu + \sin \alpha \cos \mu) \delta_r}{m V} \end{bmatrix} \triangleq \mathbf{f}_2 + \mathbf{g}_2(V, \alpha, \beta, \mu, \delta_t) \quad (16)$$

$$\dot{\mathbf{x}}_3 = \begin{bmatrix} 0 & \sin \gamma + \cos \gamma \sin \mu \tan \beta & \cos \mu \tan \beta \\ 0 & -\frac{\cos \gamma \sin \mu}{\cos \beta} & -\frac{\cos \mu}{\cos \beta} \\ 0 & \cos \gamma \cos \mu & -\sin \mu \end{bmatrix} (\mathbf{f}_2 + \mathbf{g}_2) + \begin{bmatrix} \frac{\cos \alpha}{\cos \beta} & 0 & \frac{\sin \alpha}{\cos \beta} \\ -\cos \alpha \tan \beta & 1 & -\sin \alpha \tan \beta \\ \sin \alpha & 0 & -\cos \alpha \end{bmatrix} \mathbf{x}_4 \triangleq \mathbf{f}_3 + \mathbf{g}_3 \mathbf{x}_4 \quad (17)$$

$$\dot{\mathbf{x}}_4 = \begin{bmatrix} I_1 q r + I_2 p q \\ I_5 p r + I_6 (r^2 - p^2) \\ -I_2 q r + I_8 p q \end{bmatrix} + \begin{bmatrix} I_3 & 0 & I_4 \\ 0 & I_7 & 0 \\ I_4 & 0 & I_9 \end{bmatrix} \begin{bmatrix} M_l \\ M_m \\ M_n \end{bmatrix} \quad (18)$$

where  $(V, \chi, \gamma)$  indicate the velocity, heading angle, and flight-path angle, respectively.  $(\mu, \alpha, \beta)$  are the roll angle, angle of attack, and sideslip angle, respectively.  $(p, q, r)$  are the body angular rates,  $(g, m)$  are the gravitational acceleration and UAV mass, and  $(T_{\max}, \delta_t)$  are the maximum thrust and throttle, respectively.  $I_1 = -\frac{I_z(I_x - I_y) + I_{xz}^2}{I_x I_z - I_{xz}^2}$ ,  $I_2 = \frac{I_{xz}(I_x - I_y + I_z)}{I_x I_z - I_{xz}^2}$ ,  $I_3 = \frac{I_z}{I_x I_z - I_{xz}^2}$ ,  $I_4 = \frac{I_{xz}}{I_x I_z - I_{xz}^2}$ ,  $I_5 = \frac{I_z - I_x}{I_y}$ ,  $I_6 = \frac{I_{xz}}{I_y}$ ,  $I_7 = \frac{1}{I_y}$ ,  $I_8 = \frac{I_x(I_x - I_y) + I_{xz}^2}{I_x I_z - I_{xz}^2}$ ,  $I_9 = \frac{I_x}{I_x I_z - I_{xz}^2}$ , respectively. The aerodynamic force  $(D, L, Y)$  and moment of the UAV  $(M_l, M_m, M_n)$  can be modeled as [31]

$$\begin{aligned} L &= \bar{q} S (C_{L_0} + C_{L_1}(\alpha) + C_{L_{\delta_e}} \delta_e) \\ D &= \bar{q} S (C_{D_0} + C_{D_1}(\alpha) + C_{D_{\delta_e}} \delta_e) \\ Y &= \bar{q} S (C_{Y_0} + C_{Y_{\delta_r}} \delta_r + C_{Y_{\delta_a}} \delta_a) \end{aligned} \quad (19)$$

$$\begin{aligned} M_l &= \bar{q} S \bar{b} \left( C_l(\alpha, \beta) + C_{l_{\delta_a}}(\alpha, \beta) \delta_a \right. \\ &\quad \left. + C_{l_{\delta_r}}(\alpha, \beta) \delta_r + \frac{\bar{b} p}{2V} C_{l_p} + \frac{\bar{b} r}{2V} C_{l_r} \right) \\ M_m &= \bar{q} S \bar{c} \left( C_m(\alpha, \beta) + C_{m_{\delta_e}}(\alpha, \beta) \delta_e + \frac{\bar{c} q}{2V} C_{m_q} \right) \\ M_n &= \bar{q} S \bar{b} \left( C_n(\alpha, \beta) + C_{n_{\delta_a}}(\alpha, \beta) \delta_a \right. \\ &\quad \left. + C_{n_{\delta_r}}(\alpha, \beta) \delta_r + \frac{\bar{b} p}{2V} C_{n_p} + \frac{\bar{b} r}{2V} C_{n_r} \right) \end{aligned} \quad (20)$$

where  $(\delta_e, \delta_a, \delta_r)$  indicate the elevator, aileron, and rudder deflections,  $(\bar{q}, S)$  are the dynamic pressure and

characteristic area,  $(\bar{b}, \bar{c})$  are the lateral/longitudinal characteristic lengths of the UAV, respectively, and  $(C_{L_0}, C_{L_1}, \dots, C_{n_r})$  are aerodynamic coefficients. Note that the aerodynamic forces have the following conditions:

$$\begin{aligned} L &> |Y| > 0 \\ \frac{\partial L}{\partial \alpha} &> \frac{\partial D}{\partial \alpha} > 0, \quad L > D > 0 \end{aligned} \quad (21)$$

In the aerodynamic moments, the rudder contributes yawing moment more than the aileron does, whereas the aileron contributes rolling moment more than the rudder does. That is

$$C_{l_{\delta_a}} > C_{l_{\delta_r}}, \quad C_{n_{\delta_a}} < C_{n_{\delta_r}} \quad (22)$$

These aerodynamic properties are used to design the controller in this study. In comparison with [25], in which the inertial position is the control variable, the vector  $\mathbf{x}_2$  is considered as an output to design a flight-path angle and speed controller in this study.

### III. GUIDANCE DESIGN

#### A. Deck-Motion Compensation

This section presents a DMC logic using a prediction of the carrier motion. Let us define the seakeeping state  $\mathbf{x}_s = [x_{\text{surge}} \ y_{\text{sway}} \ z_{\text{heave}} \ \phi_s \ \theta_s \ \psi_s]^T$ . During the *approach and descent phase*, only the *maneuvering* motion of the carrier is considered, and the perturbation motion caused by the wave excitation is neglected. Considering the constant glide-slope angle  $\lambda_c = \lambda_{gs}$ ,  $\eta_c = \eta_{gs}$  and the seakeeping state  $\dot{\mathbf{x}}_s = 0$ , the deck motion during the *approach and descent phase* can be estimated as

$$\begin{aligned} \hat{\mathbf{r}}_s(t) &= \mathbf{r}_{s, \text{cm}}(t_0) + \mathbf{V}_{\text{maneuver}} t + \hat{\mathbf{r}}_{s, \text{seakeep}} \\ \hat{\mathbf{r}}_{s, \text{seakeep}} &= \begin{bmatrix} y_{\text{sway}}(t_0) \cos \chi_s - x_{\text{surge}}(t_0) \sin \chi_s \\ y_{\text{sway}}(t_0) \sin \chi_s + x_{\text{surge}}(t_0) \cos \chi_s \\ z_{\text{heave}}(t_0) \end{bmatrix} \\ &\quad + \mathbf{R}(t_0) \mathbf{r}_{s/cm} \end{aligned} \quad (23)$$

In the *touchdown phase*, the *seakeeping* motion leads to the deviation of the carrier deck position. Let us introduce  $\mathbf{v}_s = [v_{\text{surge}}, v_{\text{sway}}, v_{\text{heave}}, v_{\phi}, v_{\theta}, v_{\psi}]$ , then the *seakeeping* motion in (2) can be approximated as [8], [19], [32]

$$\frac{d}{dt} \begin{bmatrix} \mathbf{x}_s \\ \dot{\mathbf{x}}_s \end{bmatrix} = \begin{bmatrix} 0 & I_6 \\ -D_s & -A_s \end{bmatrix} \begin{bmatrix} \mathbf{x}_s \\ \dot{\mathbf{x}}_s \end{bmatrix} + \begin{bmatrix} G_s \\ -G_s A_s \end{bmatrix} \mathbf{v}_s \quad (24)$$

where  $I_6$  is  $6 \times 6$  identity matrix,  $D_s = \text{diag}\{d_1, d_2, \dots, d_6\}$ ,  $A_s = \text{diag}\{a_1, a_2, \dots, a_6\}$ ,  $G_s = \text{diag}\{g_1, g_2, \dots, g_6\}$ , and  $(g_i, a_i, d_i)$  are coefficients that consist of the amplitude and natural frequency. Let us define a time-to-touchdown  $t_{\text{touch}} = t_f - t$ . The states at time-to-touchdown can be propagated as [19]

$$\hat{\mathbf{x}}_f = \Phi(t + t_{\text{touch}}, t) \hat{\mathbf{x}}_s(t) \quad (25)$$

where  $\Phi(t + t_{\text{touch}}, t)$  is a transition matrix in (24), which is given by

$$\Phi(t + t_{\text{touch}}, t) = \begin{bmatrix} \phi_{11} & \phi_{12} \\ \phi_{21} & \phi_{22} \end{bmatrix} \quad (26)$$

$$\begin{aligned} \phi_{11} &= \text{diag} \left\{ e^{(-a_1/2)t_{\text{touch}}} \cos \beta_1 t_{\text{touch}}, \dots, \right. \\ &\quad \left. e^{(-a_6/2)t_{\text{touch}}} \cos \beta_6 t_{\text{touch}} \right\} \\ \phi_{12} &= \text{diag} \left\{ e^{(-a_1/2)t_{\text{touch}}} (1/\beta_1) \sin \beta_1 t_{\text{touch}}, \dots, \right. \\ &\quad \left. e^{(-a_6/2)t_{\text{touch}}} (1/\beta_6) \sin \beta_6 t_{\text{touch}} \right\} \\ \phi_{21} &= \text{diag} \left\{ e^{(-a_1/2)t_{\text{touch}}} (-d_1/\beta_1) \sin \beta_1 t_{\text{touch}}, \dots, \right. \\ &\quad \left. e^{(-a_6/2)t_{\text{touch}}} (-d_6/\beta_6) \sin \beta_6 t_{\text{touch}} \right\} \\ \phi_{22} &= \text{diag} \left\{ e^{(-a_1/2)t_{\text{touch}}} (\cos \beta_1 t_{\text{touch}} \right. \\ &\quad \left. - (a_1/2\beta_1) \sin \beta_1 t_{\text{touch}}), \dots, e^{(-a_6/2)t_{\text{touch}}} \right. \\ &\quad \left. (\cos \beta_6 t_{\text{touch}} - (a_6/2\beta_6) \sin \beta_6 t_{\text{touch}}) \right\} \quad (27) \end{aligned}$$

The seakeeping state at the expected touchdown time  $\mathbf{x}_s(t_f)$  can be predicted. For example, the predicted pitch and heave motion of the carrier center can be obtained as

$$\begin{aligned} \hat{z}_{\text{heave}_f} &= \exp(-a_3/2)t_{\text{touch}} \\ &\quad \times ([\cos b_3 t_{\text{touch}} + (a_3/2b_3) \sin b_3 t_{\text{touch}}] z_{\text{heave}}(t) \\ &\quad + (1/b_3) \sin b_3 t_{\text{touch}} \dot{z}_{\text{heave}}(t)) \\ \hat{\theta}_{s_f} &= \exp(-a_5/2)t_{\text{touch}} \\ &\quad \times ([\cos b_5 t_{\text{touch}} + (a_5/2b_5) \sin b_5 t_{\text{touch}}] \theta_s(t) \\ &\quad + (1/b_5) \sin b_5 t_{\text{touch}} \dot{\theta}_s(t)) \quad (28) \end{aligned}$$

where  $b_3 = d_3 - a_3^2/4$ , and  $b_5 = d_5 - a_5^2/4$ . By substituting the predicted states into (3), the predicted motion at the carrier deck can be obtained as

$$\begin{aligned} \hat{\mathbf{r}}_{s_{\text{seakeep}_f}} &= \begin{bmatrix} \hat{y}_{\text{sway}_f} \cos \chi_s - \hat{x}_{\text{surge}_f} \sin \chi_s \\ \hat{y}_{\text{sway}_f} \sin \chi_s + \hat{x}_{\text{surge}_f} \cos \chi_s \\ \hat{z}_{\text{heave}_f} \end{bmatrix} \\ &\quad + \hat{\mathbf{R}}_f \mathbf{r}_{s/\text{cm}} \quad (29) \end{aligned}$$

where  $\hat{\mathbf{R}}_f = \mathbf{R}(\hat{\phi}_{s_f}, \hat{\theta}_{s_f}, \hat{\psi}_{s_f})$  is a predicted directional cosine matrix, and  $(\hat{x}_{\text{surge}_f}, \hat{y}_{\text{sway}_f}, \hat{\phi}_{s_f}, \hat{\psi}_{s_f})$  are predicted values of the seakeeping states. To provide a smooth transition input, the carrier deck model can be obtained as

$$\hat{\mathbf{r}}_s(t) = \hat{\mathbf{r}}_{s_{\text{cm}}}(t_1) + \mathbf{V}_{\text{maneuver}} \Delta t + \hat{\mathbf{r}}_{s_{\text{seakeep}_f}} (1 - e^{-\tau_s \Delta t}) \quad (30)$$

where  $\tau_s$  is a transition time constant,  $\Delta t = t - t_1$  and  $t_1$  is an initial time at *touchdown phase*. Note that the terminal glide-path angle commands should be corrected by reflecting the deck attitude at the touchdown, and therefore, the glide-slope commands are obtained as follows:

$$\begin{aligned} \lambda_c &= \lambda_c(t_1) - \hat{\theta}_{s_f} (1 - e^{-\tau_s \Delta t}) \\ \eta_c &= \eta_c(t_1) - \hat{\psi}_{s_f} (1 - e^{-\tau_s \Delta t}) \quad (31) \end{aligned}$$

Using (30) and (31), the carrier deck position  $\hat{\mathbf{r}}_s$  and the glide slope  $\lambda_c$  can be smoothly corrected to the predicted touchdown position and modified glide path. The DMC

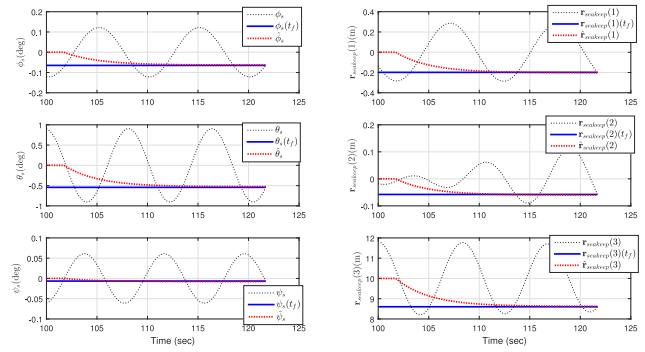


Fig. 3. Deck motion and predicted deck motion in *touchdown phase*.

utilizes the predicted deck position, and the reference trajectory is generated for the UAV to follow the predicted position with modified glide-path angles in *touchdown phase*. Fig. 3 shows the deck motion and its predicted results in a particular sea state scenario. As shown in Fig. 3, the pitch and heave motion are the major perturbation motions at the desired touchdown position. During *touchdown phase*, the predicted attitudes and displacements at the touchdown position denoted by red dotted lines appropriately converge to the values denoted by blue solid lines at the touchdown instant.

## B. Reference Trajectory Design

This section designs a reference trajectory for the UAV to capture the relative glide path that moves along with the carrier. Consider a reference point  $\mathbf{r}_{\text{ref}}$  that descends toward the carrier along the glide path, as shown in Fig. 2. The vector  $\mathbf{r}_{\text{ref}}$  can be represented as

$$\mathbf{r}_{\text{ref}} = \mathbf{r}_s + \mathbf{r}_{\text{ref}/s} \quad (32)$$

Differentiating (32) with respect to  $t$  gives the velocity of the reference point as

$$\begin{aligned} \dot{\mathbf{r}}_{\text{ref}} &= \mathbf{V}_s + \dot{\mathbf{r}}_{\text{ref}/s} \\ &= \mathbf{V}_s + \frac{\partial \mathbf{r}_{\text{ref}/s}}{\partial d_c} \dot{d}_c + \frac{\partial \mathbf{r}_{\text{ref}/s}}{\partial \lambda_c} \dot{\lambda}_c + \frac{\partial \mathbf{r}_{\text{ref}/s}}{\partial \eta_c} \dot{\eta}_c \quad (33) \end{aligned}$$

The reference trajectory is to choose an appropriate moving point, and therefore, the reference trajectory can be used to determine  $(\dot{d}_c, \dot{\lambda}_c, \dot{\eta}_c)$ . To obtain  $\dot{d}_c$ , let us take the norm of (33) as

$$\dot{d}_c^2 + a_1 \dot{d}_c + a_2 = 0 \quad (34)$$

where

$$\begin{aligned} a_1 &= 2 \frac{\mathbf{r}_{\text{ref}/s}^T}{\partial d_c} \mathbf{V}_s \\ a_2 &= -\|\dot{\mathbf{r}}_{\text{ref}}\|^2 + \|\mathbf{V}_s\|^2 + d_c^2 (\dot{\lambda}_c^2 + \dot{\eta}_c^2) \\ &\quad + 2 \mathbf{V}_s^T \left( \frac{\partial \mathbf{r}_{\text{ref}/s}}{\partial \lambda_c} \dot{\lambda}_c + \frac{\partial \mathbf{r}_{\text{ref}/s}}{\partial \eta_c} \dot{\eta}_c \right) \quad (35) \end{aligned}$$

Note that  $(\frac{\partial \mathbf{r}_{\text{ref}/s}}{\partial d_c})^T \frac{\partial \mathbf{r}_{\text{ref}/s}}{\partial d_c} = 1$ ,  $(\frac{\partial \mathbf{r}_{\text{ref}/s}}{\partial \lambda_c})^T \frac{\partial \mathbf{r}_{\text{ref}/s}}{\partial \lambda_c} = d_c^2$ ,  $(\frac{\partial \mathbf{r}_{\text{ref}/s}}{\partial \eta_c})^T \frac{\partial \mathbf{r}_{\text{ref}/s}}{\partial \eta_c} = d_c^2$ . Now, the relative closing speed  $\dot{d}_c$  can be

obtained by solving (34) as

$$\dot{d}_c = -\frac{\mathbf{r}_{\text{ref}/s}^T \mathbf{V}_s}{\partial d_c} \pm \sqrt{\left(\frac{\mathbf{r}_{\text{ref}/s}^T \mathbf{V}_s}{\partial d_c}\right)^2 - a_2} \quad (36)$$

The reference point should descend to the touchdown point for the landing, which means that  $\dot{d}_c$  should be selected as a negative real value. Assuming that the UAV maintains a constant speed  $\|\dot{\mathbf{r}}_{\text{ref}}\| = V_{\text{ref}}$  during the landing and the carrier does not turn its heading angle  $\chi_s$ , i.e., constant  $\lambda_c$  and  $\eta_c$ , (33)–(36) can be simplified as

$$\dot{\mathbf{r}}_{\text{ref}} = \mathbf{V}_s + \frac{\partial \mathbf{r}_{\text{ref}/s}}{\partial d_c} \dot{d}_c \quad (37)$$

$$\dot{d}_c^2 + 2 \frac{\partial \mathbf{r}_{\text{ref}/s}}{\partial d_c}^T \mathbf{V}_s \dot{d}_c + (\|\mathbf{V}_s\|^2 - V_{\text{ref}}^2) = 0 \quad (38)$$

Because the UAV speed is faster than the carrier speed, the relative closing velocity  $\dot{d}_c$  can be made negative. The solution of (38) can be written as

$$\dot{d}_c = -\frac{\partial \mathbf{r}_{\text{ref}/s}}{\partial d_c}^T \mathbf{V}_s - \sqrt{\left(\frac{\partial \mathbf{r}_{\text{ref}/s}}{\partial d_c}^T \mathbf{V}_s\right)^2 + (V_{\text{ref}}^2 - \|\mathbf{V}_s\|^2)} \quad (39)$$

Because the UAV flies along the line of a straight glide path, the time-to-touchdown can be estimated using the following simple equation:

$$\hat{t}_{\text{touch}} = -\frac{d_c}{\dot{d}_c} \quad (40)$$

**REMARK 1:** If the speed of the UAV and carrier heading change in approach phase, then the modified model considering those effects can be used instead of (37)–(39). However, in this study, the landing sequence and the reference trajectory are made based on the conventional landing sequence in the landing officer manual. In the sequence, the carrier normally sails into the prevailing wind to maximize the value of “wind over deck,” which determines the direction of the carrier to be constant. Upon the stabilized heading of the ship, the aircraft is regulated to maintain its speed and descent angle (glide-path angle) during the approach phase. For the reason, most of the ACLS were designed assuming the constant speed and the fixed heading of the ship [8], [12], [33].

Fig. 4 summarizes the algorithm of proposed DMC and reference trajectory generation schemes for the ACLS. In the *approach and descent phase*, unexcited carrier position and desired glide-path angles are provided from the deck motion estimator, and the trajectory is generated to make the UAV follow a stabilized glide-path angles while keeping constant speed. When the UAV gets close to the carrier (*touchdown phase*), the touch-down position  $\hat{\mathbf{r}}_s(t_f)$  is predicted and the desired glide-path angles are corrected as (31). Finally, the reference trajectory is generated according to the predicted carrier motion.

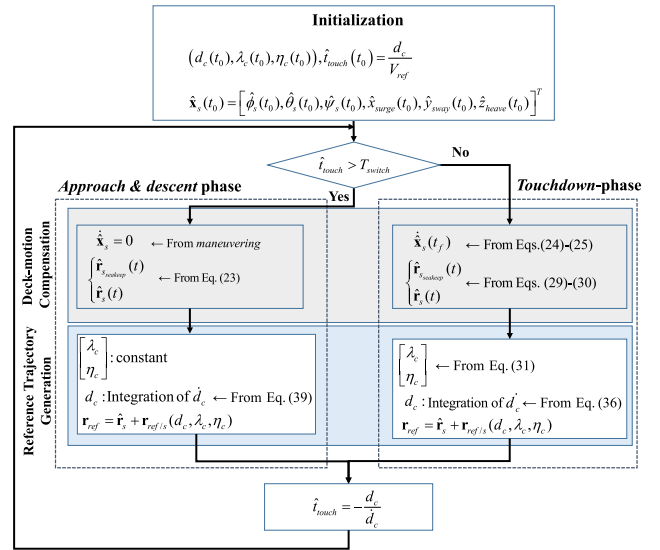


Fig. 4. Algorithm of DMC and reference trajectory generation for ACLS.

### C. Guidance Law

This section designs a nonlinear landing-guidance law using the SMC scheme for ACLS. The design objective of the guidance law is to generate guidance commands  $(V_c, \gamma_c, \chi_c)$  to track the reference trajectory  $\mathbf{r}_{\text{ref}}$ . To do that, the UAV should follow the reference trajectory  $\mathbf{r}_{\text{ref}}$  by tracking  $(d_c, \lambda_c, \eta_c)$ , and therefore, the tracking problem can be converted to the regulation of  $\mathbf{e}_1 = \mathbf{x}_1 - \mathbf{x}_{1c}$ . To track the desired  $\mathbf{x}_1$  precisely, the following proportional-integral-type sliding surface is introduced

$$\mathbf{s}_1 = \left(\frac{d}{dt} + \lambda_I\right) \int \mathbf{e}_1 dt \quad (41)$$

where  $\lambda_I$  is a positive constant. Taking the time derivative of the sliding surface gives

$$\dot{\mathbf{s}}_1 = \mathbf{f}_1 + \mathbf{g}_1 \mathbf{v}(\mathbf{x}_2) + \lambda_I \mathbf{e}_1 - \dot{\mathbf{x}}_{1c} \quad (42)$$

To analyze the closed-loop stability, introduce the following Lyapunov candidate function

$$V_{\text{GL}} = \frac{1}{2} \mathbf{s}_1^T \mathbf{s}_1 \quad (43)$$

Differentiating (43) with respect to  $t$  yields

$$\dot{V}_{\text{GL}} = \mathbf{s}_1^T \{\mathbf{f}_1 + \mathbf{g}_1 \mathbf{v}(\mathbf{x}_2) + \lambda_I \mathbf{e}_1 - \dot{\mathbf{x}}_{1c}\} \quad (44)$$

The desired dynamics of the sliding surface is proposed as

$$\dot{\mathbf{s}}_1 = -K_1 \mathbf{s}_1 - K_2 |\mathbf{s}_1|^{\alpha_1} \text{sign}(\mathbf{s}_1) \quad (45)$$

where  $1 > \alpha_1 > 0$  and  $K_1, K_2 > 0$  are design parameters. The parameter  $K_1$  contributes the exponential convergence of the sliding surface, and the parameters  $\alpha_1$  and  $K_2$  are related to the finite-time convergence to the sliding surface. To ensure that the sliding surface dynamics of (42) satisfy (45), a pseudo-guidance input  $\mathbf{v} = [v_1 \ v_2 \ v_3]^T$  can be

selected as

$$\mathbf{v} = \mathbf{M}((-\mathbf{f}_1 + \dot{\mathbf{x}}_{1c} - \lambda_l \mathbf{e}_1 - K_1 \mathbf{s}_1 - K_2 |\mathbf{s}_1|^{\alpha_1} \text{sign}(\mathbf{s}_1)) \quad (46)$$

Consequently, the time derivative of the Lyapunov candidate function becomes negative definite, and the dynamic system is asymptotically stable in  $\mathcal{D} = \{\mathbf{s}_1 : \mathbf{s}_1 = 0\}$

$$\begin{aligned} \dot{V}_{GL} &= \mathbf{s}_1^T \{-K_1 \mathbf{s}_1 - K_2 |\mathbf{s}_1|^{\alpha_1} \text{sign}(\mathbf{s}_1)\} \\ &= -2K_1 V_{GL} - 2K_2 V_{GL}^{(\alpha_1+1)/2} < 0 \end{aligned} \quad (47)$$

REMARK 2: Despite the advantage of finite-time convergence, chattering phenomenon may happen due to signum function in the guidance law. To deal with the problem, a boundary-layer approximation can be used to replace the sign function [21], [25], [27]. In this study, the saturation function is adopted as a boundary-layer approximation, which eliminates the infinite frequency switching near the desired sliding surfaces.

Using the inverse mapping of  $\mathbf{h}_1$ , the guidance commands  $V_c$ ,  $\gamma_c$ , and  $\chi_c$  can be determined as

$$V_c = \|\mathbf{v}\|, \quad \gamma_c = -\sin^{-1}\left(\frac{v_3}{\|\mathbf{v}\|}\right), \quad \chi_c = \tan^{-1}\left(\frac{v_2}{v_1}\right) \quad (48)$$

#### IV. CONTROLLER DESIGN

##### A. Outer Loop Controller

This section designs a flight-path controller for ACLS. The objective of the control loop is to make the UAV track the guidance commands  $(V_c, \chi_c, \gamma_c)$  while keeping a zero sideslip ( $\beta_c = 0$ ) during the maneuver. Consider the sliding surface vectors of

$$\mathbf{s}_2 = \begin{bmatrix} \left(\frac{d}{dt} + k_1\right)^2 \int \mathbf{e}_2 dt \\ \left(\frac{d}{dt} + k_1\right) \int e_\beta dt \end{bmatrix} \quad (49)$$

where  $\mathbf{e}_2 = \mathbf{x}_2 - \mathbf{x}_{2c}$  and  $e_\beta = \beta - \beta_c$ . Note that the second derivative of  $\mathbf{x}_2$  is needed to obtain the time derivative of the sliding surface of (49). To design the controller, the following assumptions are introduced.

Assumption 1: The aerodynamic forces contributed by the control surfaces are neglected.

Assumption 2: The lumped uncertainties included in the system dynamics are bounded.

Assumption 3: The angle-of-attack and the side-slip angle of the UAV are bounded by

$$\mathcal{A} = \{(\alpha, \beta) : 0 < \alpha_L \leq \alpha \leq \alpha_H, |\beta| < \beta_H < \pi/4\}$$

The main objective of the control surfaces of the UAV is to generate control moments for attitude control, and therefore, Assumption 1 is widely used in the design of the aircraft controller [25], [26]. Assumption 2 is also valid because the wind disturbance that constitutes the uncertainty is bounded during the operation. Assumption 3 designates a flight envelope of the UAV during aircraft landing. In general, most of the aircraft use positive angle-of-attack

while capturing an descending glide-slope or an altitude. In addition, the carrier chooses its heading to prevent drastic side-wind on the deck. Using Assumption 1, the neglected terms are considered as uncertainties. The second-order dynamics of  $\mathbf{x}_2$  can be obtained by taking the time derivative of (16) as

$$\begin{aligned} \ddot{\mathbf{x}}_2 &= \left\{ \left( \frac{\partial \mathbf{f}_2}{\partial \mathbf{x}_2} + \frac{\partial \mathbf{g}_2}{\partial \mathbf{x}_2} \right) (\mathbf{f}_2 + \mathbf{g}_2) + \frac{\partial \mathbf{g}_2}{\partial \mathbf{x}_3} \mathbf{f}_3 \right\} \\ &\quad + \left[ \frac{\partial \mathbf{g}_2}{\partial \delta_l} \quad \frac{\partial \mathbf{g}_2}{\partial \mathbf{x}_3} \mathbf{g}_3 \right] \begin{bmatrix} \dot{\delta}_{lc} \\ \mathbf{x}_4 \end{bmatrix} + \Delta_1 \\ &\triangleq \mathbf{F}_2 + \mathbf{G}_2 \mathbf{u}_{OL} + \Delta_1 \end{aligned} \quad (50)$$

where  $\mathbf{u}_{OL} = [\dot{\delta}_{lc} \quad \mathbf{x}_4]^T$ , and  $\Delta_1$  is a lumped uncertainty of  $\dot{\mathbf{x}}_2$  dynamics. Differentiating (49) and substituting (17) and (50) into the resultant equation yields the sliding surface dynamics represented in an input-affine form

$$\begin{aligned} \dot{\mathbf{s}}_2 &= \begin{bmatrix} \mathbf{F}_2 + 2k_1 \dot{\mathbf{e}}_2 + k_1^2 \mathbf{e}_2 - \ddot{\mathbf{x}}_{2c} \\ f_\beta + k_1 e_\beta \end{bmatrix} + \begin{bmatrix} \mathbf{G}_2 \\ \mathbf{g}_\beta \end{bmatrix} \mathbf{u}_{OL} \\ &\quad + \begin{bmatrix} \Delta_1 \\ \Delta_\beta \end{bmatrix} \triangleq \mathbf{F}_{s_2} + \mathbf{G}_{s_2} \mathbf{u}_{OL} + \Delta_s \end{aligned} \quad (51)$$

where  $f_\beta = \mathbf{e}_3^T \mathbf{f}_3$ ,  $\mathbf{e}_3 = [0 \ 0 \ 1]^T$ ,  $\mathbf{g}_\beta = [0 \ \sin \alpha \ 0 \ -\cos \alpha]$ , and  $\Delta_\beta$  are defined from (17). From Assumption 2, the lumped uncertainty of  $\Delta_s$  is bounded as  $\|\Delta_s\| \leq \bar{\Delta}_s$ . Invertibility of the matrix  $\mathbf{G}_{s_2}$  is proved in Appendix A. To analyze the stability of the outer loop system, introduce the following Lyapunov candidate function:

$$V_{OL} = \frac{1}{2} \mathbf{s}_2^T \mathbf{s}_2 \quad (52)$$

Differentiating (52) with respect to  $t$  and substituting (51) into the resultant equation yields

$$\dot{V}_{OL} = \mathbf{s}_2^T (\mathbf{F}_{s_2} + \mathbf{G}_{s_2} \mathbf{u}_{OL} + \Delta_s) \quad (53)$$

To make the outer loop system converge to the above sliding surface, the control input  $\mathbf{u}_{OL}$  is obtained as

$$\mathbf{u}_{OL} = \mathbf{G}_{s_2}^{-1} (-\mathbf{F}_{s_2} - K_3 \mathbf{s}_2 - K_4 \text{sign}(\mathbf{s}_2)) \quad (54)$$

where  $K_3$  and  $K_4$  are positive gains. Substituting (54) into (53) yields

$$\begin{aligned} \dot{V}_{OL} &= \mathbf{s}_2^T (-K_3 \mathbf{s}_2 - K_4 \text{sign}(\mathbf{s}_2) + \Delta_s) \\ &\leq -2K_3 V_{OL} - \|\mathbf{s}_2\|_2 (K_4 - \bar{\Delta}_s) \end{aligned} \quad (55)$$

To compensate for the uncertainty,  $K_4$  is selected as  $K_4 = \kappa_1 + \bar{\Delta}_s$ , where  $\kappa_1 > 0$ . Thus, the time derivative of the Lyapunov candidate function can be made negative-definite, which means that the control input renders the outer loop system asymptotically stable as

$$\dot{V}_{OL} \leq -2K_3 V_{OL} - 2\kappa_1 \sqrt{V_{OL}} < 0 \quad (56)$$

##### B. Inner loop Controller

The angular rate controller is designed as an inner loop controller to make the attitude rate of the UAV track the attitude-rate commands  $x_{4c}$  that are generated by the outer



loop controller. Consider the sliding surface  $\mathbf{s}_3$  as

$$\mathbf{s}_3 = \left( \frac{d}{dt} + k_2 \right) \int (\mathbf{x}_4 - \mathbf{x}_{4c}) dt \quad (57)$$

To express the time derivative of the sliding surface in an input-affine form, (18) is rearranged to consider the uncertainty due to wind disturbances as, Eq. (58) shown at the bottom of this page, where  $\mathbf{u}_{IL}$  denotes a control input of the inner loop. Differentiating the sliding surface gives

$$\dot{\mathbf{s}}_3 = \mathbf{f}_4 + k_2(\mathbf{x}_4 - \mathbf{x}_{4c}) + \mathbf{g}_4 \mathbf{u}_{IL} + \Delta_4 \quad (59)$$

To investigate the inner loop stability, let us introduce the following Lyapunov candidate function:

$$V_{IL} = \frac{1}{2} \mathbf{s}_3^T \mathbf{s}_3 \quad (60)$$

Differentiating (60) with respect to  $t$  and substituting (59) into the resulting equation yields

$$\dot{V}_{IL} = \mathbf{s}_3^T \{ \mathbf{f}_4 + k_2(\mathbf{x}_4 - \mathbf{x}_{4c}) + \mathbf{g}_4 \mathbf{u}_{IL} + \Delta_4 \} \quad (61)$$

To make the inner loop system converge to the above sliding surface, the control input  $\mathbf{u}_{IL}$  is obtained as

$$\mathbf{u}_{IL} = \mathbf{g}_4^{-1} \{ -\mathbf{f}_4 - k_2(\mathbf{x}_4 - \mathbf{x}_{4c}) - K_5 \mathbf{s}_3 - K_6 \text{sign}(\mathbf{s}_3) \} \quad (62)$$

where  $K_5$  and  $K_6$  are positive gains. The invertibility of the matrix  $\mathbf{g}_4$  is also found in Appendix B. Substituting (62) into (61) yields

$$\begin{aligned} \dot{V}_{IL} &= \mathbf{s}_3^T \{ -K_5 \mathbf{s}_3 - K_6 \text{sign}(\mathbf{s}_3) + \Delta_4 \} \\ &\leq -2K_5 V_{IL} - \|\mathbf{s}_3\|_2 (K_6 - \bar{\Delta}_4) \end{aligned} \quad (63)$$

where  $\|\Delta_4\| \leq \bar{\Delta}_4$  by Assumption 2. To compensate for the uncertainty, the gain  $K_6$  is selected as  $K_6 = \kappa_2 + \bar{\Delta}_4$ , where  $\kappa_2 > 0$ . Using the selected gain, the time derivative of the Lyapunov candidate function can be made negative-definite as

$$\dot{V}_{IL} \leq -2K_5 V_{IL} - 2\kappa_2 \sqrt{V_{IL}} < 0 \quad (64)$$

Therefore, the closed-loop system is asymptotically stable. Note that the sign function in the control input can be replaced by the saturation function to mitigate the chattering phenomenon. Also note that although the magnitude of the lumped uncertainties  $\Delta_s$  and  $\Delta_4$  are not clearly known in the control design process, their magnitudes do not exceed

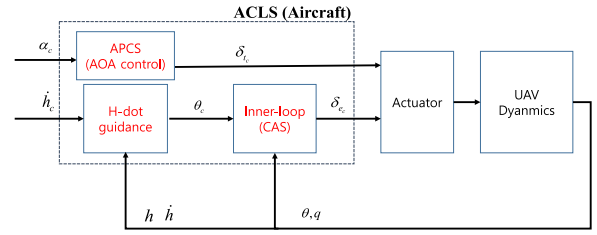


Fig. 5. Architecture of the conventional ACLS [8].

50% of the nominal dynamics in the high seas. By choosing the upper bounds as  $\bar{\Delta}_s = 0.5\|\mathbf{F}_{s2}\|$  and  $\bar{\Delta}_2 = 0.5\|\mathbf{f}_4\|$ , the design parameters  $K_4$  and  $K_6$  can be chosen accordingly.

## V. NUMERICAL RESULTS

To demonstrate the performance of the proposed guidance and control system for the ACLS, numerical simulations are performed for two different scenarios. The first scenario is to validate the proposed guidance and controller by comparison with the conventional guidance and control design in [8]. Because the conventional approach was designed only for the longitudinal motion, only the vertical plane is considered for the simulation. The architecture of the conventional ACLS is shown in Fig. 5 and control laws and parameters are summarized in Table I. In the simulation, the carrier moves north with a constant speed. A marshal point that represents the starting point in the *approach phase* is located on the line of the glide slope, and the distance between the marshal point and the carrier  $d_{c0}$  is chosen as 5000 m. The initial UAV position is randomly selected within a specified area around the marshal point. The desired reference trajectory is initially located at the marshal point and moves toward the carrier deck along with the glide path. The initial conditions for scenario 1 are summarized in Table II, where *rand* (1) represents the random number uniformly distributed between [0 1]. In the second scenario, a 3-D landing simulation considering the sea state is carried out to demonstrate the performance using the proposed DMC algorithm. The horizontal glide-path angle is selected to satisfy the design requirement. The initial conditions for scenario 2 are summarized in Table III. In the

$$\begin{aligned} \dot{\mathbf{x}}_4 &= \left\{ \begin{bmatrix} I_1 q r + I_2 p q \\ I_5 p r + I_6 (r^2 - p^2) \\ -I_2 q r + I_8 p q \end{bmatrix} + \bar{q} S \begin{bmatrix} I_3 & 0 & I_4 \\ 0 & I_7 & 0 \\ I_4 & 0 & I_9 \end{bmatrix} \begin{bmatrix} \bar{b} \left( C_l(\alpha, \beta) + \frac{\bar{b} p}{2V} C_{l_p} + \frac{\bar{b} r}{2V} C_{l_r} \right) \\ \bar{c} \left( C_m(\alpha, \beta) + \frac{\bar{c} q}{2V} C_{m_q} \right) \\ \bar{b} \left( C_n(\alpha, \beta) + \frac{\bar{b} p}{2V} C_{n_p} + \frac{\bar{b} r}{2V} C_{n_r} \right) \end{bmatrix} \right\} \\ &\quad + \bar{q} S \begin{bmatrix} I_3 & 0 & I_4 \\ 0 & I_7 & 0 \\ I_4 & 0 & I_9 \end{bmatrix} \begin{bmatrix} 0 & \bar{b} C_{l_{\delta a}}(\alpha, \beta) & \bar{b} C_{l_{\delta r}}(\alpha, \beta) \\ \bar{c} C_{m_{\delta e}}(\alpha, \beta) & 0 & 0 \\ 0 & \bar{b} C_{n_{\delta a}}(\alpha, \beta) & \bar{b} C_{n_{\delta r}}(\alpha, \beta) \end{bmatrix} \begin{bmatrix} \delta_e \\ \delta_a \\ \delta_r \end{bmatrix} + \begin{bmatrix} \Delta_p \\ \Delta_q \\ \Delta_r \end{bmatrix} \\ &\triangleq \mathbf{f}_4 + \mathbf{g}_4 \mathbf{u}_{IL} + \Delta_4 \end{aligned} \quad (58)$$

TABLE I  
Simulation Parameters for the Conventional ACLS

	Control law	Design parameters
H-dot guidance	$\theta_c = K_h h_e + K_{\dot{h}} \dot{h}_e + K_{\ddot{h}} \ddot{h}_e$	$K_h = 0.5, K_{\dot{h}} = 1.4, K_{\ddot{h}} = 0.4$
Inner-loop (CAS)	$\delta_e = K_\theta \frac{s+0.1\omega}{s+\omega_1} \theta_e + K_q q$	$K_\theta = 0.1, \omega = 20, K_q = 0.1$
APC [2]	$\delta_t = K_\alpha \alpha_e + K_{\alpha_I} \frac{1}{s} \alpha_e + K_n a_N$	$K_\alpha = 5, K_{\alpha_I} = 2, K_n = -0.02$

TABLE II  
Initial Conditions for Automatic Carrier Landing Simulations: Scenario 1

Parameter description	Symbol	Values	Units
Initial carrier position, speed	$(\mathbf{r}_s(0), V_s)$	(0, 0, 10)	m, m/s
glide-path angle command	$\lambda_c$	3.5	deg
flight-path angle command([8])	$\gamma_c$	3.5	deg
distance from marshal point	$d_{c0}$	5000	m
Initial UAV position	$\mathbf{r}_{uav}(0)$	$d_{c0}(\cos\lambda_c, \sin\lambda_c \pm 20rand(1))$	m
Initial UAV speed	$V(0)$	51	m/s

TABLE III  
Initial Conditions For Automatic Carrier Landing Simulations: Scenario 2

Parameter description	Symbol	Values	Units
Initial carrier position (NED)	$\mathbf{r}_s(0)$	(0, 0, 0)	m
carrier speed, heading	$(V_s, \psi_s)$	(10, 0)	m/s, deg
glide-path angle commands	$(\lambda_c, \eta_c)$	(3.5, 173)	deg
distance from marshal point	$d_{c0}$	5000	m
Initial UAV position (NED)	$\mathbf{r}_{uav}(0)$	$\mathbf{r}_{ref}(0) \pm rand(1)(0, 50, 20)$	m
Initial UAV speed, heading	$(V(0), \chi(0))$	(51, 0)	m/s, deg

simulation, the actuator dynamics is considered

$$\frac{\delta_i}{\delta_c} = \frac{20^2}{s^2 + (0.707)20s + 20^2} \quad (65)$$

$$\frac{\delta_t}{\delta_{tc}} = \frac{2}{s + 2} \quad (66)$$

where  $i \in [\text{Rudder, Aileron, Elevator}]$ . For the control surface  $\delta_i$ , the amplitude limit and the rate limit are set as  $20^\circ$  and  $60^\circ/\text{s}$ , respectively. For the engine, the amplitude limit and the rate limit are set as  $[0 \ 1]$  and  $1/\text{s}$ , respectively.

#### A. Comparison With Conventional ACLS

The simulation results using the conventional ACLS and the proposed ACLS are compared in Fig. 6(a). Under calm weather conditions, both ACLS systems provide good tracking performance. To track the moving glide path while keeping  $\lambda_c$ , both guidance loops generate commands to make the flight-path angle  $\gamma$  smaller than the glide-path angle  $\lambda$ . In the proposed ACLS, the flight-path angle command  $\gamma_c$  and speed command  $V_c$  are properly generated so that they simultaneously converge to the moving glide-path angle with the desired approaching speed. The UAV speed and flight-path angle are directly controlled by the proposed nonlinear controller, such that the UAV follows the glide path and reaches the carrier deck successfully by tracking the guidance commands. In the conventional approach, compared with the proposed ACLS system, large transient errors are involved, and the ACLS that uses a throttle command for compensating for the error in the angle of attack yields the tracking error of the UAV speed. Fig. 6(b)

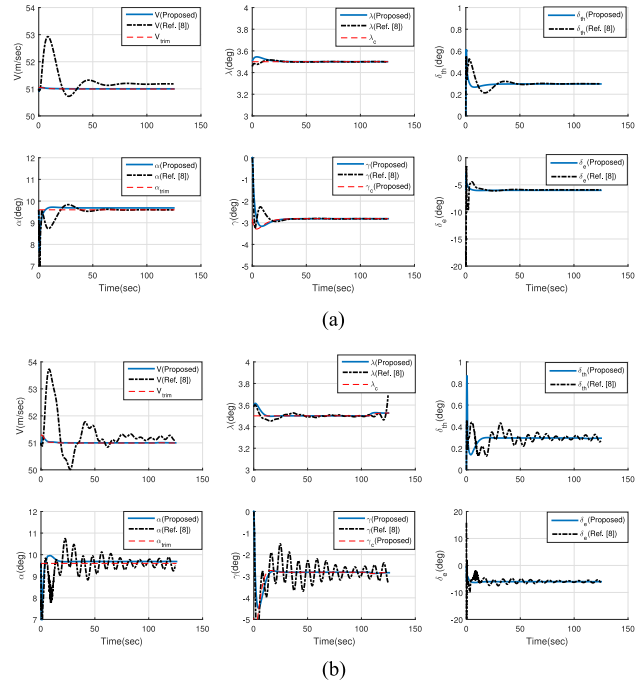


Fig. 6. Simulation results: Scenario 1, Comparison with Conventional ACLS. (a) Time responses using proposed ACLS and conventional ACLS ( $V_s = 10 \text{ m/s}$ , Sea state 0). (b) Time responses using proposed ACLS and conventional ACLS ( $V_s = 10 \text{ m/s}$ , Sea state 3).

shows the simulation results under sea state 3. Under the wave-exciting condition, the conventional ACLS degrades the tracking performance. The deviated carrier position is directly fed back into the H-dot autopilot without utilizing DMC from the shipboard signal, which incorporates

TABLE IV  
Simulation Results: Longitudinal Touchdown Error from the  
Touchdown Point

		Proposed	Ref. [8]
Touchdown error(m)	Sea state 0	0.002	-0.02
	Sea state 3	0.026	1.24

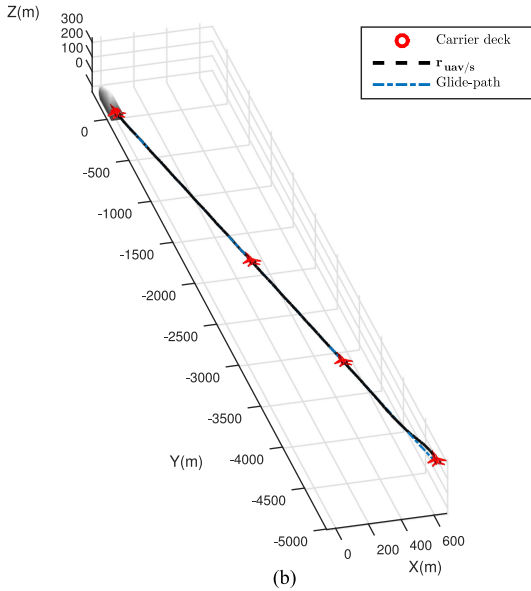
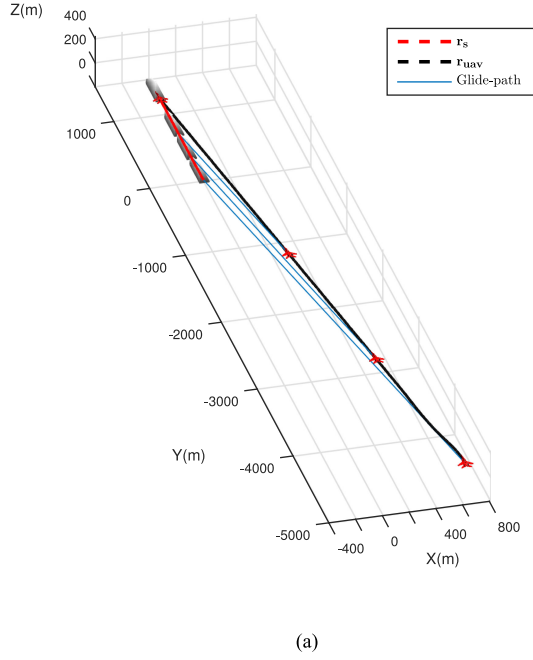


Fig. 7. Carrier landing scenario 2: 3-D carrier landing scenario (Sea state 0). (a) Trajectories of UAV and carrier. (b) Relative trajectory of UAV.

oscillatory responses of the flight-path angle as well as the angle of attack and speed and increases the touchdown error, as shown in Table IV. If the carrier encounters a more severe sea state (over sea state 3), the performance is expected to be worse. Upon using the proposed ACLS, on the other hand, it is observed that the UAV responses are less

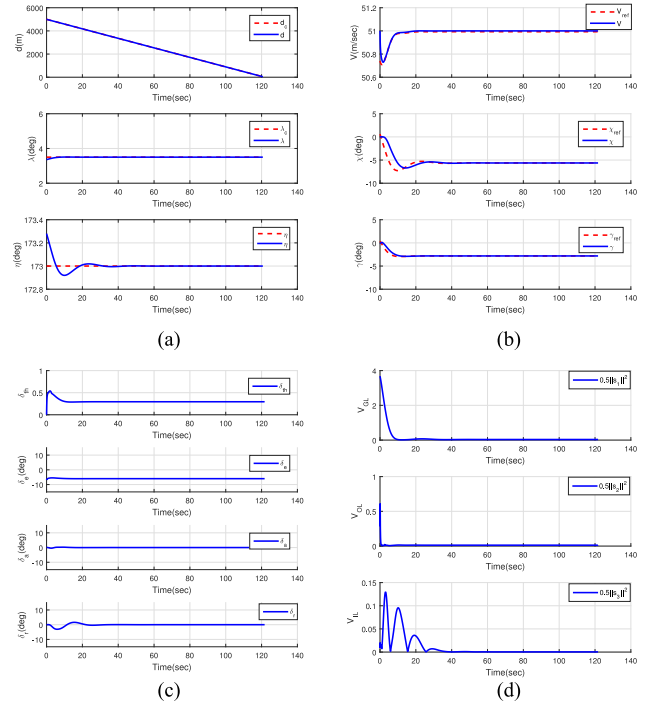


Fig. 8. Carrier landing scenario 2: 3-D carrier landing scenario (Sea state 0). (a) Time histories of distance, line-of-sight angles. (b) Time histories of  $V$ ,  $\chi$ , and  $\gamma$ . (c) Time histories of control inputs. (d) Time histories of the Lyapunov functions.

sensitive to the heave motion throughout the maneuver. By using the proposed DMC in the guidance law, the final deck motion is properly predicted in the *touchdown phase*, and the proposed ACLS improves the touchdown accuracy, as shown in Fig. 6(b).

## B. Carrier Landing Scenario in 3-D Space

1) *Landing Under Calm Weather Conditions*: To demonstrate the performance of the proposed guidance and controller in 3-D space, a numerical simulation is carried out. Figs. 7 and 8 show the simulation results conducted under sea state 0. As shown in Fig. 7(a), the UAV approaches the carrier deck, keeping a line-of-sight that coincides with the desired glide-path angle. In view of the carrier frame, the UAV captures and descends through the relative glide path, as shown in Fig. 7(b). Fig. 8 shows the time histories of the UAV during landing. The guidance commands are properly generated to capture the desired trajectory, as shown in Fig. 8(a), and the speed, flight-path angle, and heading angle of the UAV converge to the guidance commands, achieving a safe landing on the desired touchdown point.

2) *Landing Under the High Sea State (Sea state 5)*: In this scenario, the proposed ACLS with the DMC algorithm is compared to the proposed ACLS without DMC for the high sea state environment. In the scenario, a constant wind that blows from the northwest (north: 5 m/s, west: 5 m/s) is considered to be uncertain, and 100 ms delayed signals transmitted from the shipboard system are considered. Fig. 9 shows the simulation results. Compared to the

TABLE V  
Touchdown Dispersion Results: Location From the Touchdown Point

		Sea state			
		Sea state 3, wind: 5m/s		Sea state 5, wind: 10m/s	
with DMC	Mean(m)	(2.75,-0.33)	(3.20,-0.45)	(1.83,-0.23)	(4.18,-0.58)
	RMS(m)	(3.04,0.35)	(5.48,0.72)	(4.39,0.58)	(7.49,0.96)
	Accurate landing ratio(%)	98%	95%	93%	82%
without DMC	Mean(m)	(3.85,-0.46)	(4.06,-0.54)	(2.23,-0.19)	(-4.72,0.50)
	RMS(m)	(6.75,0.90)	(7.26,0.94)	(9.18,1.21)	(20.38, 2.53)
	Accurate landing ratio(%)	92%	89%	82%	49%

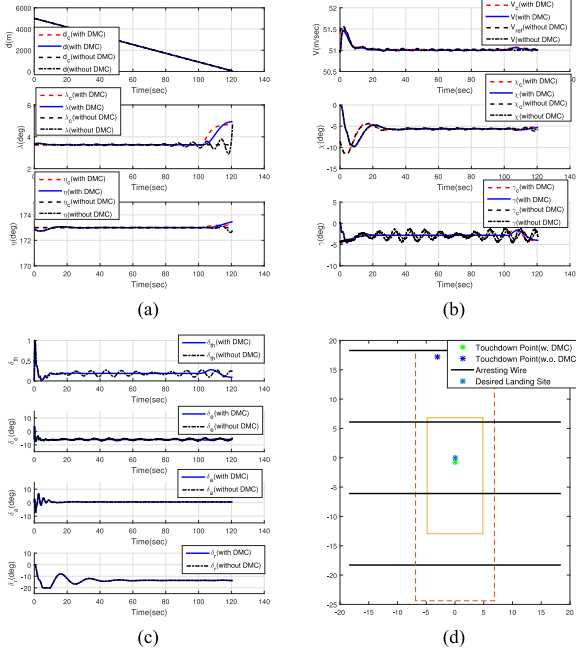


Fig. 9. Carrier landing scenario 2: 3-D carrier landing scenario (Sea state 5, with delayed ship signal). (a) Time histories of distance, line-of-sight angles. (b) Time histories of  $V$ ,  $\chi$ , and  $\gamma$ . (c) Time histories of control inputs. (d) Touchdown Dispersion.

results under calm weather conditions, the ACLS without DMC shows oscillatory responses during the landing due to the *seakeeping* motion at the carrier deck. The unstabilized and delayed motion causes a large touchdown error from the desired landing site. The proposed ACLS, on the other hand, exhibits smooth responses in the *approach and descent* phase because the stabilized signal of the carrier deck position transmitted from the DMC is used in the guidance loop. In the *touchdown phase*, the predicted touchdown position and desired glide-slope commands are successfully compensated. As a result, the UAV using DMC could land on the landing site within the desired accuracy under the existence of the delayed shipboard signal.

3) *Monte Carlo Simulation*: To demonstrate the robustness of the proposed ACLS, hundreds of Monte Carlo simulations are executed for various sea states, where a wind-disturbance model (MIL-STD-8785C, [29]) and delayed shipboard signals randomly chosen from 10 to 100 ms are considered in the simulation to reflect the actual environment. Fig. 10 shows the touchdown dispersion from the

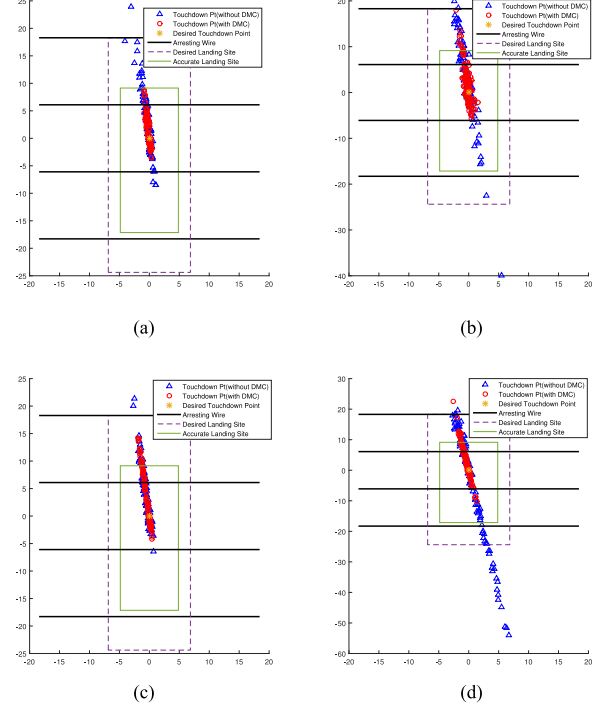


Fig. 10. Simulation results for carrier landing scenario 3: Touchdown dispersion. (a) Sea state 3, without delayed shipboard signal. (b) Sea state 5, without delayed shipboard signal. (c) Sea state 3, with delayed shipboard signal. (d) Sea state 5, with delayed shipboard signal.

landing site, with the results summarized in Table V, where mean and rms represent the average touchdown error and root-mean-square errors, and accurate landing ratio denotes the proportion of accurate landings with respect to the number of landing attempts. Under calm weather conditions, the ACLS without DMC and the proposed ACLS achieve precision landing with small dispersions from the desired landing spot. As the weather condition gets worse, the ACLS without DMC experiences increased dispersion errors, and some cases even fail to land. The proposed ACLS using DMC, on the other hand, has a small touchdown dispersion from the desired landing spot, even in harsh weather conditions, and most cases (95%) succeed in achieving a precision landing, as shown in Table V. The time-delay signal has a greater effect on the landing as the sea state becomes severe. Without DMC, the touchdown errors increase significantly when the shipboard signal is delayed under sea state 5. On the other hand, using the DMC, the touchdown dispersion was



formed within acceptable range and did not increase much as the sea state increased. Based on the results, it can be concluded that the proposed ACLS achieves accurate landing performance even in harsh weather condition and signal delay condition.

## VI. CONCLUSION

A sliding mode based nonlinear guidance and control method was proposed for an UAV automatic landing system on a carrier. To accomplish precise landing, 3-D landing kinematics was derived by taking the relative motion of the carrier into account. The guidance commands were generated to compensate for the relative glide path, which were used in the inner loop autopilot, and a nonlinear controller was designed for the ACLS. Numerical simulations were performed to demonstrate the performance of the proposed guidance and control system. Simulation results showed satisfactory tracking performance, and the guidance law integrated with the autopilot system can be utilized for the UAV landing on the carrier even in high sea state. For further work, an autopilot for a fully automatic recovery system including takeoff, waveoff, and bolter maneuvers can be designed, and a decision-making process to evaluate the landing risks and determine the landing policy can be integrated into the ACLS.

## APPENDIX

### A. INVERTIBILITY OF $G_{s_2}$

Matrix  $G_{s_2}$  can be expressed as the multiplication of two matrices as

$$G_{s_2} = \begin{bmatrix} \frac{\partial g_2}{\partial \delta_t} & \frac{\partial g_2}{\partial \mathbf{x}_3} & g_3 \\ 0 & e_3^T & g_3 \end{bmatrix} = \begin{bmatrix} \frac{\partial g_2}{\partial \delta_t} & \left[ \frac{\partial g_2}{\partial \mu} & \frac{\partial g_2}{\partial \alpha} & \frac{\partial g_2}{\partial \beta} \right] \\ 0 & [0 \ 0 \ 1] \end{bmatrix} \begin{bmatrix} 1 & \mathbf{0}_{1 \times 3} \\ \mathbf{0}_{3 \times 1} & g_3 \end{bmatrix} \triangleq \Xi \Theta \quad (\text{A.1})$$

where  $\frac{\partial g_2}{\partial \delta_t}$  and  $\frac{\partial g_2}{\partial \mathbf{x}_3} = [\frac{\partial g_2}{\partial \mu} \ \frac{\partial g_2}{\partial \alpha} \ \frac{\partial g_2}{\partial \beta}]$  are given by

$$\begin{aligned} \frac{\partial g_2}{\partial \delta_t} &= T_{\max} \begin{bmatrix} \frac{\cos \alpha \cos \beta}{m} \\ \frac{\sin \alpha \sin \mu - \cos \alpha \sin \beta \cos \mu}{m V \cos \gamma} \\ \frac{\cos \alpha \sin \beta \sin \mu + \sin \alpha \cos \mu}{m V} \end{bmatrix} \\ \frac{\partial g_2}{\partial \mu} &= \begin{bmatrix} 0 \\ \frac{Y \sin \mu + L \cos \mu + T_{\max} \delta_t (\sin \alpha \cos \mu + \cos \alpha \sin \beta \sin \mu)}{m V \cos \gamma} \\ \frac{Y \cos \mu - L \sin \mu + T_{\max} \delta_t (\cos \alpha \sin \beta \cos \mu - \sin \alpha \sin \mu)}{m V} \end{bmatrix} \\ \frac{\partial g_2}{\partial \alpha} &= \begin{bmatrix} \frac{-\partial D / \partial \alpha - T_{\max} \delta_t \sin \alpha \cos \beta}{m} \\ \frac{\partial L / \partial \alpha \sin \mu + T_{\max} \delta_t (\cos \alpha \sin \mu + \sin \alpha \sin \beta \cos \mu)}{m V \cos \gamma} \\ \frac{\partial L / \partial \alpha \cos \mu + T_{\max} \delta_t (-\sin \alpha \sin \beta \sin \mu + \cos \alpha \cos \mu)}{m V} \end{bmatrix} \quad (\text{A.2}) \end{aligned}$$

To check the invertibility of the  $G_{s_2}$ , let us consider the determinant of the matrix  $\Xi$ , Eq. (A.3) and (A.4) shown at the bottom of this page, Since  $L > |Y| > 0$ ,  $\frac{\partial L}{\partial \alpha} > \frac{\partial D}{\partial \alpha} > 0$ , and  $0 < \alpha_L < \alpha < \alpha_H$ ,  $|\beta| < \beta_H < \pi/4$ , terms in (A.5) have the following inequalities:

$$\begin{aligned} T \frac{\partial D}{\partial \alpha} (1 - \cos^2 \alpha \cos^2 \beta) &> 0 \\ \cos \alpha \left( L \frac{\partial L}{\partial \alpha} \cos \beta + Y \frac{\partial D}{\partial \alpha} \sin \beta \right) &> 0 \\ T \cos \alpha \sin \alpha \left( T + \frac{\partial L}{\partial \alpha} \right) &> 0 \\ L \left( T \cos \beta + \frac{\partial D}{\partial \alpha} \sin \alpha \right) &> 0 \quad (\text{A.5}) \end{aligned}$$

$$\begin{aligned} \det(\Xi) &= \det \left( \begin{bmatrix} \frac{\partial g_2}{\partial \delta_t} & \frac{\partial g_2}{\partial \mu} & \frac{\partial g_2}{\partial \alpha} \\ 0 & 0 & 1 \end{bmatrix} \right) \\ &= \frac{T_{\max}}{m^3 V^2 \cos \gamma} \times \\ &\quad \begin{vmatrix} \cos \alpha \cos \beta & 0 & -\partial D / \partial \alpha - T_{\max} \delta_t \sin \alpha \cos \beta \\ \sin \alpha \sin \mu - \cos \alpha \sin \beta \cos \mu & Y \sin \mu + L \cos \mu + T_{\max} \delta_t & \partial L / \partial \alpha \sin \mu + T_{\max} \delta_t \\ \cos \alpha \sin \beta \sin \mu + \sin \alpha \cos \mu & Y \cos \mu - L \sin \mu + T_{\max} \delta_t & \partial L / \partial \alpha \cos \mu + T_{\max} \delta_t \end{vmatrix} \\ &\quad \times (\sin \alpha \cos \mu + \cos \alpha \sin \beta \sin \mu) \times (\cos \alpha \sin \mu + \sin \alpha \sin \beta \cos \mu) \\ &\quad \times (\cos \alpha \sin \beta \cos \mu - \sin \alpha \sin \mu) \times (-\sin \alpha \sin \beta \sin \mu + \cos \alpha \cos \mu) \end{vmatrix} \quad (\text{A.3}) \end{aligned}$$

which yields

$$\begin{aligned} \det(\Xi) &= \frac{T_{\max}}{m^3 V^2 \cos \gamma} \left( T \frac{\partial D}{\partial \alpha} + T^2 \sin \alpha \cos \beta + L T \cos \beta + L \frac{\partial D}{\partial \alpha} \sin \alpha - T \frac{\partial D}{\partial \alpha} \cos^2 \alpha \cos^2 \beta \right. \\ &\quad \left. + L \frac{\partial L}{\partial \alpha} \cos \alpha \cos \beta + Y \frac{\partial D}{\partial \alpha} \cos \alpha \sin \beta + T \frac{\partial L}{\partial \alpha} \cos \alpha \cos \beta \sin \alpha \right) \quad (\text{A.4}) \end{aligned}$$

Therefore, the determinant  $\Xi$  is always positive during the landing. On the other hand,  $\det(\Theta)$  can be written as

$$\det(\Theta) = \left[ \begin{array}{c|c} 1 & \mathbf{0}_{1 \times 3} \\ \hline \mathbf{0}_{3 \times 1} & g_3 \end{array} \right] \\ = \det(g_3) = -\sec \beta \neq 0 \quad (\text{A.6})$$

Therefore,  $G_{s_2}$  is always nonsingular.

## B. INVERTIBILITY OF $g_4$

From (58),  $g_4$  can be expressed as

$$g_4 = \bar{q}S \begin{bmatrix} I_3 & 0 & I_4 \\ 0 & I_7 & 0 \\ I_4 & 0 & I_9 \end{bmatrix} \\ \times \begin{bmatrix} 0 & \bar{b}C_{l_{\delta a}}(\alpha, \beta) & \bar{b}C_{l_{\delta r}}(\alpha, \beta) \\ \bar{c}C_{m_{\delta e}}(\alpha, \beta) & 0 & 0 \\ 0 & \bar{b}C_{n_{\delta a}}(\alpha, \beta) & \bar{b}C_{n_{\delta r}}(\alpha, \beta) \end{bmatrix} \\ \triangleq \mathbf{J}\Psi \quad (\text{B.1})$$

The determinant of  $g_4$  is equivalent to the determinants of each matrices  $\mathbf{J}$  and  $\Psi$ . First, let us consider the determinant of the inertia matrix  $\mathbf{J}$

$$\det(\mathbf{J}) = \left[ \begin{array}{c|c} I_3 & 0 & I_4 \\ \hline 0 & I_7 & 0 \\ I_4 & 0 & I_9 \end{array} \right] = I_7 (I_3 I_9 - I_4^2) \quad (\text{B.2})$$

By substituting  $I_7 = I_y^{-1}$ ,  $I_3 = \frac{I_z}{I_x I_z - I_{xz}^2}$ ,  $I_4 = \frac{I_{xz}}{I_x I_z - I_{xz}^2}$ ,  $I_9 = \frac{I_x}{I_x I_z - I_{xz}^2}$  into (B.2), it can be written as

$$\det(\mathbf{J}) = \frac{1}{(I_x I_z - I_{xz}^2) I_y} \neq 0 \quad (\text{B.3})$$

Next, the determinant of the matrix  $\Psi$  can be expressed as

$$\det(\Psi) = (\bar{q}S)^3 \bar{c} \bar{b}^2 \\ \times \left[ \begin{array}{c|c|c} 0 & C_{l_{\delta a}}(\alpha, \beta) & C_{l_{\delta r}}(\alpha, \beta) \\ \hline C_{m_{\delta e}}(\alpha, \beta) & 0 & 0 \\ \hline 0 & C_{n_{\delta a}}(\alpha, \beta) & C_{n_{\delta r}}(\alpha, \beta) \end{array} \right] \\ = -(\bar{q}S)^3 \bar{c} \bar{b}^2 C_{m_{\delta e}} (C_{l_{\delta a}} C_{n_{\delta r}} - C_{l_{\delta r}} C_{n_{\delta a}}) \quad (\text{B.4})$$

From the aerodynamic moments of the UAV, i.e.,  $C_{l_{\delta a}} > C_{l_{\delta r}}$ ,  $C_{n_{\delta a}} < C_{n_{\delta r}}$ ,  $\Psi$  and  $g_4$  are nonsingular.

## REFERENCES

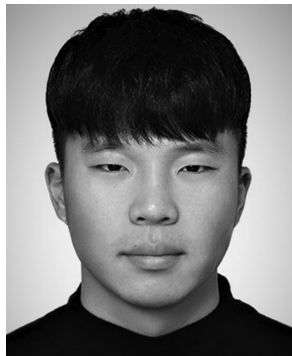
- [1] D. Smith  
*One Hundred Years of U.S. Navy Air Power*. Annapolis, MD, USA: Naval Institute Press, 2013.
- [2] S. J. Craig, R. F. Ringland, and I. L. Ashkenas  
An analysis of navy approach power compensator problems  
*J. Aircraft*, vol. 9, no. 10, pp. 737–743, 1972.
- [3] J. M. Urnes, R. K. Hess, R. F. Moomaw, and R. W. Huff  
H-dot automatic carrier landing system for approach control in turbulence  
*J. Guid., Control, Dyn.*, vol. 4, no. 2, pp. 177–183, 1981.
- [4] J. L. Crassidis, D. J. Mook, and J. M. McGrath  
Automatic carrier landing system utilizing aircraft sensors  
*J. Guid., Control, Dyn.*, vol. 16, no. 5, pp. 914–921, 1993.
- [5] Z. Qi-Dan, W. Tong, Z. Xun-Yu, and Z. Fang  
Adaptive variable structure guidance system design of a longitudinal automatic carrier landing system  
*In Proc. Chin. Control Decis. Conf.*, Guilin, China, Nov. 2009, pp. 4855–4859.
- [6] J. D. Bošković and J. Redding  
An autonomous carrier landing system for unmanned aerial vehicles  
*In Proc. AIAA Guid., Navig., Control Conf.*, Chicago, IL, USA, Aug. 2009, pp. 1–17.
- [7] S. Lee, H. Choi, Y. Kim, S. Kim, S. Kim, and J. Suk  
Unmanned aerial vehicles glide-path-angle-tracking for autonomous carrier landing  
*In Proc. Asia-Pac. Int. Symp. Aerosp. Technol.*, Shanghai, China, Sep. 2014, pp. 1–12.
- [8] J. M. Urnes and R. K. Hess  
Development of the F/A-18a automatic carrier landing system  
*J. Guid., Control, Dyn.*, vol. 8, no. 3, pp. 289–295, 1985.
- [9] R. W. Huff and G. K. Kessler  
Enhanced displays, flight controls and guidance systems for approach and landing  
Naval Air Test Center, Patuxent River, MD, USA, Tech. Rep. AD/A244869, 1991.
- [10] M. B. Subrahmanyam  
H-infinity design of F/A-18a automatic carrier landing system  
*J. Guid., Control, Dyn.*, vol. 17, no. 1, pp. 187–191, 1994.
- [11] R. Niewoehner and I. I. Kaminer  
Design of an autoland controller for an F-14 aircraft using H-infinity synthesis  
*J. Guid., Control, Dyn.*, vol. 19, no. 3, pp. 656–663, 1996.
- [12] M. Steinberg and A. Page  
A comparison of neural, fuzzy, evolutionary, and adaptive approaches for carrier landing  
*In Proc. AIAA Guid., Navig., Control Conf.*, Montreal, QC, Canada, Aug. 2001, pp. 1–12.
- [13] Y. Deng and H. Duan  
Control parameter design for automatic carrier landing system via pigeon-inspired optimization  
*Nonlinear Dyn.*, vol. 85, pp. 97–106, 2016.
- [14] J. Li and H. Duan  
Simplified brain storm optimization approach to control parameter optimization in F/A-18 automatic carrier landing system  
*Aerosp. Sci. Technol.*, vol. 42, pp. 187–195, 2015.
- [15] G. Xia, R. Dong, J. Xu, and Q. Zhu  
Linearized model of carrier-based aircraft dynamics in final-approach air condition  
*J. Aircraft*, vol. 53, no. 1, pp. 33–47, 2016.
- [16] R. A. Hess and M. Judd  
Improved automatic carrier landing using deck motion prediction  
*J. Aircraft*, vol. 13, no. 2, pp. 153–155, 1976.
- [17] A. Katre  
Ship state and covariance propagation using time series analysis and forecasting  
M.S. thesis, Dept. Mech. Aerosp. Eng., Illinois Inst. Technol., Chicago, IL, USA, 2014.
- [18] A. Khan, C. Bil, and K. Marion  
Ship motion prediction for launch and recovery of air vehicles  
*In Proc. OCEANS MTS/IEEE*, Washington, DC, USA, Sep. 2005, pp. 2795–2801.
- [19] M. Sidar and B. Doolin  
On the feasibility of real-time prediction of aircraft carrier motion at sea  
*IEEE Trans. Autom. Control*, vol. 28, no. 3, pp. 350–356, Mar. 1983.
- [20] X. Zhao, R. Xu, and C. Kwan  
Ship-motion prediction: Algorithms and simulation results  
*In Proc. IEEE Int. Conf. Acoust., Speech, Signal Process.*, Montreal, QC, Canada, May 2004, pp. 125–128.

- [21] T. Shima, M. Idan, and O. M. Golan  
Sliding-mode control for integrated missile autopilot guidance  
*J. Guid., Control, Dyn.*, vol. 29, no. 2, pp. 250–260, 2006.
- [22] H. Xu, M. D. Mirmirani, and P. A. Ioannou  
Adaptive sliding mode control design for a hypersonic flight vehicle  
*J. Guid., Control, Dyn.*, vol. 27, no. 5, pp. 829–838, 2004.
- [23] S. Islam and P. X. Liu  
Robust sliding mode control for robot manipulators  
*IEEE Trans. Ind. Electron.*, vol. 58, no. 6, pp. 2444–2453, Jun. 2011.
- [24] J. Bae and Y. Kim  
Adaptive controller design for spacecraft formation flying using sliding mode controller and neural networks  
*J. Franklin Inst.*, vol. 349, no. 2, pp. 578–603, 2012.
- [25] S. N. Singh, M. L. Steinberg, and A. B. Page  
Nonlinear adaptive and sliding mode flight path control of F/A-18 model  
*IEEE Trans. Aerosp. Electron. Syst.*, vol. 39, no. 4, pp. 1250–1262, Oct. 2003.
- [26] C. I. Ahn, Y. Kim, and H. J. Kim  
Adaptive sliding mode controller design for fault tolerant flight control system  
In *Proc. AIAA Guid., Navig., Control Conf.*, Keystone, CO, USA, Aug. 2006, pp. 1–10.
- [27] R. A. Hess  
Frequency domain-based pseudosliding mode flight control design  
*J. Aircr.*, vol. 49, no. 6, pp. 2077–2088, 2012.
- [28] S. Eastburg  
NATOPS landing signal officer manual  
US Dept. of the Navy, Naval Air Systems Command, Rept. NAVAIR 00-80T-104, Patuxent River, MD, 2004.
- [29] J. F. Sweger  
Design specifications development for unmanned aircraft carrier landings: A simulation approach  
United States Naval Acad., Annapolis, MD, USA, Trident Scholar Project Rep. 316, 2003.
- [30] T. Perez  
*Ship Motion Control: Course Keeping and Roll Stabilisation Using Rudder and Fins*. London, U.K.: Springer, 2006.
- [31] O. Park, S. Kim, J. Suk, and G. Lee  
Study on nonlinear modeling for medium altitude unmanned aerial vehicle  
In *Proc. Korea Soc. Aeronautical Space Sci. Fall Conf.*, Jeju, South Korea, Nov. 2014, pp. 492–495.
- [32] T. Durand and R. J. Wasicko  
Factors influencing glide path control in carrier landing  
*J. Aircr.*, vol. 4, no. 2, pp. 146–158, 1967.
- [33] M. Steinberg  
Development and simulation of an F/A-18 fuzzy logic automatic carrier landing system  
In *Proc. 2nd IEEE Int. Conf. Fuzzy Syst.*, San Francisco, CA, USA, Mar. 1993, pp. 797–802.



**Seokwon Lee** received the B.S. degree in aerospace engineering in 2012 from the Department of Mechanical and Aerospace Engineering, Seoul National University, Seoul, South Korea, where he is currently working toward the Ph.D. degree.

His research interests include nonlinear flight control, and missile guidance and control.



**Jihoon Lee** received the B.S. degrees in mechanical engineering and astronomy from Yonsei University, Seoul, South Korea, in 2014. He is currently working toward the Ph.D. degree with the Department of Mechanical and Aerospace Engineering, Seoul National University, Seoul, South Korea.

His research interests include robust and gain-scheduled control, control of linear parameter-varying systems, and modeling and control of morphing aircraft.



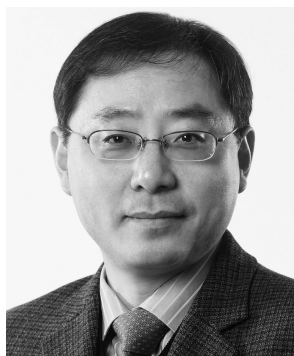
**Somang Lee** received the Bachelor degree in mechanical and aerospace engineering in 2014 from Seoul National University, Seoul, South Korea, where he is currently working toward the Ph.D. degree in aerospace engineering.

His main research interests include air-traffic management and fault detection isolation and reconfiguration.



**Hyunjin Choi** received the Ph.D. degree in aerospace engineering from the Department of Mechanical and Aerospace Engineering, Seoul National University, Seoul, South Korea, in 2014.

He is currently a Research Engineer with the Korea Aerospace Research Institute, Daejeon, South Korea. His research interests include collision avoidance of vehicles and intelligent vehicle guidance and control.



**Youdan Kim** (M'94–SM'16) received the B.S. and M.S. degrees in aeronautical engineering from Seoul National University, Seoul, South Korea, and the Ph.D. degree in aerospace engineering from Texas A&M University, College Station, TX, USA, in 1983, 1985, and 1990, respectively.

In 1992, he joined the faculty of the Seoul National University, where he is currently a Professor with the Department of Mechanical and Aerospace Engineering. His current research interests include the control system design for aircraft and spacecraft, reconfigurable flight control system, and missile guidance and control.



**Seungkeun Kim** (SM'16) received the B.S. and Ph.D. degrees in mechanical and aerospace engineering from Seoul National University, Seoul, South Korea, in 2002 and 2008, respectively.

He is currently an Associate Professor with the Department of Aerospace Engineering, Chungnam National University, Daejeon, South Korea. From April 2008 to February 2012, he was a Research Fellow and a Lecturer with Cranfield University, Cranfield, U.K. He has actively published book chapters and journal and conference papers related to unmanned aerial systems. His current research interests includes nonlinear guidance and control, estimation and sensor fusion, and decision making for micro/small aerial vehicles.



**Jinyoung Suk** received the B.S., M.S. and Ph.D. degrees in aerospace engineering from Seoul National University, Seoul, South Korea, in 1992, 1994, and 1998, respectively.

He is currently a Professor with the Department of Aerospace Engineering, Chungnam National University, Daejeon, South Korea. From 1998 to 2001, he was a Senior Researcher with Korea Aerospace Industries. His research interests cover dynamics, system identification, control, guidance, and estimation for various types of unmanned systems